Simulations of the Tenuous Upper Atmospheres of Exoplanets

Lucian Spitzner

Division of Astrophysics
Department of Physics
Lund University

2023-EXA211

Degree project of 60 higher education credits (for a degree of Master)

Supervisor: Jens Hoeijmakers

Division of Astrophysics
Department of Physics
Box 43
SE-221 00 Lund
Sweden

Abstract

Over the last decade, the interest in research on extraterrestrial planets has expanded dramatically. With the number of confirmed exoplanets having increased tenfold over the last ten years, we now know that many different types of exoplanets exist. Modern telescopes, both ground- and space-based, like the Very Large Telescope (VLT) or the James Webb Space Telescope (JWST) will drive forward the research on exoplanets discovered by missions like Kepler or TESS. Despite a present day bias towards detection of large Jupiter-like planets, a plethora of smaller, Earth-like planets are now being discovered. Research on those planets is especially interesting in the context of habitability and the search for potential extraterrestrial life. However, for most planets current technology is not precise enough to resolve light directly. Instead, the two main methods indirectly measure the effect of planets through variations in the stellar spectrum. For transiting planets, i.e. planets that orbit into the line of sight between star and observer, their shadow causes a momentary reduction in stellar flux. The reduction in flux is proportional to the ratio of planetary to stellar area. Surface conditions on planets are greatly affected by their atmospheres. A great diversity of atmospheres is known to exist, with different constituents, temperatures, chemistry and morphologies. In transmission spectroscopy, the stellar light filtered through the thin atmospheric annulus surrounding the planet is split into its spectrum to identify signatures from atoms and molecules. These can give insight about the properties of the atmospheres. However, it is not only the dense parts of atmospheres that contribute to this signal. The outer atmospheric layer, called the exosphere, is thinly populated by ionised particles, also called plasma. Many solar system bodies feature an exosphere, including Mars, Venus and Earth. The existence of exospheres has been confirmed for some exoplanets. Exospheres of planets may be very large due to strong incident stellar wind flux. Imprints of exospheric ions may be visible in transmission spectroscopy.

In this work, three-dimensional models of the extraterrestrial planet π Men c have been created using the hybrid-kinetic code AMITIS. π Men c is a roughly $2\,R_\oplus$ super-Earth in a very close orbit around a Sun-like star. Previous research by García Muñoz et al. (2021) using the Hubble Space Telescope (HST) detects absorption by C II ions in the ultraviolet, with a peak absorption depth of 6 %. According to their models, these particles surround the planet in a large, 15 planetary radii exosphere. Particles are sourced from lower parts of the atmosphere, where they are photoionised and escape into the exosphere. There, interactions with the stellar wind cause them to accelerate, which is visible in the observed transmission spectrum. García Muñoz et al. vary parameters like particle densities and ionisation timescales to match their model to observations. However, the influence of magnetic fields is not included. Hence, our approach extends their research. AMITIS includes physical processes like magnetic fields, electron pressure or stellar wind pressure to compute the time-dependant evolution of a system. Using the assumption that π Men c is similar to Venus in its atmospheric composition, we create different models of the planet. Outputs of this code include densities and velocities of particles in the exosphere. These results are then used in radiative transfer. Here, we calculate the extinction of light through the exosphere. As a result, we obtain synthetic transmission spectra. Similar to García Muñoz et al., we then vary parameters in the plasma models to fit our results to their observations.

While staying below the threshold of ion density proposed by García Muñoz et al., we are able to reach transit depths on the same order of magnitude as in the observations: With peak densities of C II around $10^{5.5}\,cm^{-3}$, a maximum transit depth of 2 % is reached for a planet with no intrinsic magnetic field. We find that magnetic fields affect the shape and position of the ion absorption lines. For a non-magnetised planet, the peak of the absorption line is shifted by about $130\,km\,s^{-1}$, while a planet with a dipole similar to Earth has peak line depth shifted by $100\,km\,s^{-1}$. Most likely, shielding by the magnetosphere decreases entrainment and acceleration of planetary ions in the stellar winds. As a result, the position of the absorption line peak relative to its intrinsic centre may hold information about the magnetic field of the exoplanet. The properties of the stellar wind also significantly affect the observed transmission spectrum. We find that a change in angle of the stellar magnetic field also changes the absorption depth by about 25 %. For close orbit planets, the orientation of the stellar magnetic field can therefore not be ignored. Variations in stellar wind intensity are expected to change the line profile as well. Over multiple observations, changes in the absorption line could be used to reveal variations of stellar winds for other stars.

Popular Science Summary

Ever since the discovery of the first exoplanet, mankind has dreamed of discovering another planet similar to Earth. These could be the key for the future of our civilisation, or the first contact with extraterrestrial life. More than 5000 planets have been discovered, and this number is expected to soar with future missions. All different kinds of exoplanet have now been discovered: Extremely large, gassy planets like Jupiter, ice giants like Neptune, but also smaller planets, more similar to Earth. These planets can be covered with dense gas, liquid oceans, or even lava. In order to find habitable planets, we need to investigate their surface conditions. These are tightly bound to the planetary atmospheres. From the solar system, we know that atmospheres change over time. It is hypothesised that the now barren red planet Mars used to have an atmosphere. But, presumably due to the loss of its magnetic field, it was unable to retain most of it. On the other hand, despite not having an intrinsic magnetic field, Venus managed to keep a thick layer of atmosphere. How exactly magnetic fields affect the evolution of atmospheres is not fully understood. It is therefore important to investigate how atmospheres lose their mass, and the role of magnetic fields.

It is incredibly difficult to directly measure light from exoplanets, even more so from their atmosphere. Instead, scientists measure the change of the stellar light as a planet orbits across the stellar disc. Of course, this is only possible for planets that transit, i.e. cross the line of sight between observer and star. The imprint of a planetary atmosphere is then detectable in the spectrum of the stellar light. This is commonly known as transmission spectroscopy. Larger planets are more easily observed with this method. And yet, modern telescopes reach unprecedented levels of resolution, which opens the field for characterisation of smaller, terrestrial exoplanets.

In this work, we investigate the planet π Men c. It is roughly double the size of Earth, but orbits around its host star 20 times closer than Earth around the Sun. This is an extreme environment: Life like on Earth would not exist here. Observations of this planet suggest that a large structure surrounds the planet, known as an exosphere. This is the uppermost layer of the atmosphere, and populated by low-density charged particles, also called plasma. This plasma is created due strong stellar irradiation. Although ionised particles are affected by magnetic fields, previous modelling work on this planet does not include them. We use a three-dimensional plasma code that includes various physical effects, including magnetic fields. This allows us to create artificial observations of the exosphere of π Men c. We can then tweak various physical parameters, like the speed of the stellar winds, or the strength of the planetary magnetic field. This causes changes in the spectrum we calculate from our models. Doing this, we try to find the best fit of parameters to reproduce observations.

We find that magnetic fields affect the observed light from atmospheres. This could be a step towards confirming the existence of extraterrestrial magnetic fields. Furthermore, we might even be able put constraints on the strength of these fields. By simulating different particles, we can make predictions about future observations. All of this will be important for other terrestrial exoplanets. Our simulation and modelling pipeline provides a new approach to investigate Earth-like planets.

We most likely will not be able to travel to other planets within our lifetime. Even more so, the planets we currently investigate are not habitable to humans. However, we help lay the groundwork for future scientists in the search of a second Earth. Without doubt, these planets exist. We just have to find them.

Contents

Acknowledgements **iii**

1 Introduction **1**
1.1 Overview of exoplanet science . . . 1
1.2 Detection and observation of exoplanets . . . 3
1.2.1 Radial velocity . . . 3
1.2.2 Transit method . . . 4
1.3 Transmission spectroscopy . . . 5
1.3.1 Exospheres . . . 5
1.4 Magnetic fields . . . 6
1.5 Close-orbit terrestrial exoplanets . . . 6
1.6 Planet π Men c . . . 7

2 Theory and Methodology **9**
2.1 Plasma model: AMITIS . . . 9
2.1.1 Atmospheric model . . . 10
2.2 Radiative transfer . . . 11
2.2.1 Atomic theory . . . 11
2.2.1.1 Atomic line theory . . . 12
2.2.1.2 Relative flux absorption . . . 13
2.2.2 Line list . . . 14
2.2.3 Prometheus . . . 14
2.2.4 Line profile and position . . . 14
2.2.5 Plasmetheus . . . 16
2.2.6 Spectral resolution and sampling . . . 16
2.2.7 Stellar spectrum . . . 16
2.3 Parker Spirals . . . 17
2.4 Fiducial run . . . 18

3 Results and Discussion **23**
3.1 π Men c . . . 23
3.1.1 Unmagnetized planet . . . 23
3.1.1.1 AMITIS results . . . 23
3.1.1.2 Plasmetheus spectra . . . 25
3.1.2 Magnetised planet . . . 25
3.1.2.1 AMITIS results . . . 25
3.1.2.2 Plasmetheus spectra . . . 26
3.1.2.3 Optical depth . . . 27
3.1.3 Parker spiral effects . . . 28

4 Conclusions **33**
4.1 Comparison to observations 33
4.2 AMITIS models 34
4.3 Ions and transitions 34
4.4 Simulation parameter space 35
4.5 Plasmetheus adaptations 35

List of Abbreviations **37**

Bibliography **39**

Appendices **43**

Acknowledgements

First and foremost I would like to thank my supervisor, Dr. Jens Hoeijmakers, for his continued support and scientific guidance. I also extend this gratitude to the two doctoral students Bibiana Prinoth and Nicolas Borsato, especially for their emotional assistance. I would like to thank Andrea Gebek for his support in the theoretical background of radiative transfer. Further I would like to thank our collaborators from Umeå, especially Prof. Maria Hamrin and Dr. Shahab Fatemi, for regular meetings, inspiring ideas and scientific support. I am thankful to Dr. Alexander Mustill for his valuable feedback on my draft.

Without my office mates in the *Pollux* office, especially John and Viktor, I'm sure this program would have seemed impossible to master. Of course, I would like to thank all master students here at Lund Observatory, for providing me with a healthy social life to balance the hours spent in front of the computer screen. The other doctoral student also deserve my gratitude, for being a link between master students and researchers. Additionally, I would like to thank the former master coordinator Dr. Florent Renaud, for admitting me to the programme and giving me the chance to study the stars.

I would like to thank my girlfriend, especially for the moral support in the final days before submission. Finally, I am incredibly grateful to my parents for making it possible for me to study in Sweden.

This research has made use of data obtained from or tools provided by the portal exoplanet.eu of *The Extrasolar Planets Encyclopaedia*.

This research has made use of the NASA Exoplanet Archive, which is operated by the California Institute of Technology, under contract with the National Aeronautics and Space Administration under the Exoplanet Exploration Program.

This research has made use of the SIMBAD database, operated at CDS, Strasbourg, France.

Chapter 1

Introduction

1.1 Overview of exoplanet science

With the knowledge about the existence of other stars in the universe followed the thought about extraterrestrial planets, which ties closely to the question of alien life. While studies of the stars may be as old as human civilisation, observing planets around other stars only became feasible in the late twentieth century. In recent years, new techniques for detection and improved apparatus with unprecedented quality and precision have caused a boom in astronomical, and more specifically exoplanetary science. By the definition of the International Astronomical Union (IAU), an exoplanet follows roughly the same definition of a planet[1]: They have to orbit a stellar object, have roughly spherical shape and clear their immediate environment of rubble, gas and dust. Exoplanets furthermore must be unable to fuse deuterium in their core (like some brown dwarfs can) and have certain mass ratio with the their host (Lecavelier des Etangs & Lissauer, 2022). Objects other than Main Sequence (MS) stars may act as a host, such as quasars, brown dwarfs and white dwarfs. Exoplanets greatly differ in their properties, covering a wide range of e.g. sizes, densities, phase states, internal structure, temperatures, metallicities and atmospheres. Evolutionary changes, such as tidal locking, orbital circularisation, atmospheric stripping or migration also affect them, further increasing the diversity in exoplanets observed today. In *The Exoplanet Handbook*, published in 2011, Perryman states that more than 500 exoplanets had been discovered. This number has increased tenfold in the last ten years. Major survey missions like the Kepler space telescope, the Wide Angle Search for Planets (WASP) and Hungarian-made Automated Telescope (HAT) greatly contributed to the number of exoplanets found. The James Webb Space Telescope (JWST), launched in December 2021 provides extensive potential for exoplanet research due to its wavelength coverage in the infrared spectrum. Understanding the possibilities of life-sustaining environments entails insight into the surface conditions of those planets.

With the detection of ever more exoplanets in our galaxy, we develop a new sense for the diversity of exoplanets, which extends beyond what was previously known. Our solar system is divided into two parts: The inner system features the terrestrial planets Mercury, Venus, Earth and Mars in a close orbit around the Sun, all within a few au's (one Astronomical Unit (au) is approximately the distance between Earth and Sun). Further out are the gas giants Jupiter and Saturn and thereafter the ice giants Uranus and Neptune. These three types of planets are unique in their chemical and molecular composition, due to different formation histories, masses and orbital distances. In contrast, observations reveal other types of exoplanets. For example, Jupiter-like planets are often found in orbits closer than Mercury around their host star. This class of planets is labelled **Hot Jupiters**. Terrestrial planets may also be found at orbital distances of a fraction of an au, and may be called **Lava Worlds**. Planets with masses between $1\,M_\oplus$ to $10\,M_\oplus$ are referred to as **super-Earths**. Planets close to their host star are prime candidates to be observed with the transit detection method (Sect. 1.2.2). On the contrary, planets similar in orbital configuration to Earth or Venus have not

[1] For the sake of simplicity, the terms "exoplanet" and "planet" may be used interchangeably throughout this work.

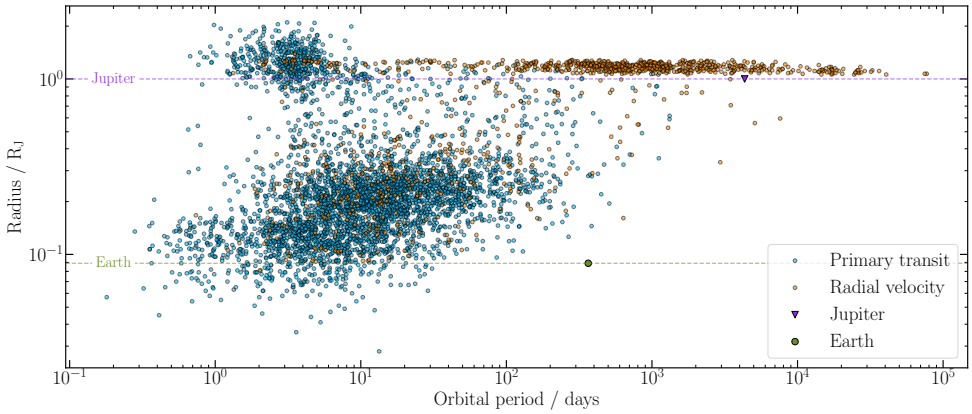

Figure 1.1: Populations of confirmed exoplanets found using the radial velocity method and the primary transit method. Together, they account for roughly 90% of confirmed exoplanets found (California Institute of Technology, 2023). Of those, almost 80% were found using the primary transit method. Terrestrial planets like Earth are still largely unable to be detected. The radius of Radial Velocity (RV) planets is calculated with mass-radius relations, which are uncertain for high planetary masses.

been found yet. However, this does not indicate some peculiarity about these planets, but rather highlights the limitations of present-day detection methods.

To answer questions that arise with the growing field of exoplanetary research, especially those connected to extraterrestrial life and habitability, a fundamental understanding of the surface conditions is essential. Spectrographs are used to further investigate the light from exoplanets. In transmission spectroscopy, the stellar light during transit (see Sect. 1.2.2) can give insight about the chemical composition and abundance of elements in exoplanetary atmospheres. Of special interest are molecules found on Earth, but also those theorised to be essential for life, among others being Oxygen (O), Carbon (C), Hydrogen (H), Water (H_2O), and Carbon Dioxide (CO_2) (Feinstein et al., 2023). An ongoing topic of research, both for our solar system and other planetary systems, is the influence of planetary magnetic fields on the atmospheres and the interactions with the circumstellar environments of the host system. For Earth, its magnetic field interacts with the solar winds, which consist of mainly ionised protons and electrons ($\approx$ 96%, Prölss, 2004). Within the Earth's ionosphere, the solar winds are the main process driving the ionisation of particles. For Venus, a planet that no longer has an intrinsic magnetic field, interactions between the incoming stellar winds and ionised particles from its upper atmosphere create an induced magnetic field (Brace & Kliore, 1991). The presence of a magnetic field may reduce the atmospheric loss of matter through interactions with the stellar winds, and thus impacts the evolution of atmospheres, and consequently surface environment (Seki et al., 2001; Driscoll & Bercovici, 2013), also (Grießmeier, 2015, Sect. 11.3).

Within this work, we use results from a three-dimensional magneto-hydrodynamical model of small, terrestrial-sized planets in close orbits, together with two different codes to create synthetic transmission spectra of exoplanetary exospheres. These predictive spectra are created for Ultraviolet (UV) and optical wavelengths. We investigate the effect of different parameters of the model used, for example particle source rates, magnetic field strengths or stellar wind intensity. In doing so, we follow up on previous research on magnetic fields of exoplanets (García Muñoz et al., 2021; Ben-Jaffel et al., 2022). Moreover, we intend to investigate the possibility of detection of these environments with current and future telescopes. Hence, we aim to gain insight into the parameter space of scenarios between exoplanets and their host stars, specifically the interactions between the stellar winds, magnetic fields, and atmospheric constituents.

1.2 Detection and observation of exoplanets

The first detection of an exoplanet by Wolszczan & Frail (1992) was accomplished through a method now known as pulsar timing. Through slight variations in well-known regular radio signals from pulsars, the orbital time and the planetary mass can be calculated. Waves at radio frequency are more easily observed that in the optical, since they are not subject to atmospheric aberrations, and can be obtained independant of time and weather. Since 1992, our technological ability to detect exoplanets has improved greatly. And yet, detections of exoplanets still usually do not measure light directly emitted by the planet, but rather light from the host star. The planet's influence on the star and its spectrum are measured indirectly. Modern telescopes can reach a sufficiently high spatial resolution to directly resolve the light emitted by planets. Because the flux of the host star is usually orders of magnitudes greater than that of the planet, a coronagraph is used to block the stellar light. Due to the limitations by telescope aberrations, direct imaging is limited to bright, giant gas planets oftentimes hundreds of au from their host star. For planets in closer orbits, the two main detection methods today are the RV method and the transit method. The highest informational gain is obtained from combining parameters from measurements of both methods. Radial velocity and transit measurements complement each other. For example, the Gaia space telescope can obtain both radial velocity and transit measurements for stars, but furthermore also measures the planet-induced "wobble" of the star. This requires high precision astrometric data, either by space-based telescopes or ground-based telescopes with adaptive optics (Liu et al., 2008; Leggett et al., 2019; Mainzer et al., 2011). In the Gaia data release 3, Gaia Collaboration et al. (2022) found several new exoplanet candidates, as well as some confirmations [2].

1.2.1 Radial velocity

The motion within stellar systems follow Newton's laws. Two masses (planet and star) will rotate around the common centre of mass, called the barycentre. Whereas the effect of the host on the planet is usually significantly greater than that of the planet on the star, the star nonetheless revolves around the barycentre with the same period as the planet. Absorption lines in the stellar spectrum may appear at different wavelengths due to the stars movement relative to the observer. This planet-induced **Doppler-shift** represents the change in RV of the star relative to the observer. In 1995, Mayor & Queloz used the RV method to discover the first planet orbiting a MS star. One limit for the radial velocity method is set by planet mass: The smaller the planet, the smaller is also the induced movement of the host star around the barycentre. Therefore, planets with larger masses are more likely to be found. When the mass of the star is known, one may infer a lower boundary for the planetary mass, as well as orbital period and eccentricity. For a given system of star and planet, the measured radial velocity is greatest when it is observed edge on, and zero for a face-on observation. For the same reason, the mass measured by RV observations is dependant on the inclination i between the line of sight and the orbital plane of the planet, and denoted as $M \sin(i)$. Nonetheless, because the detection of a single planet takes multiple spectroscopic observations of the star, only about a fifth of confirmed exoplanets have been first detected with the radial velocity method (Exoplanet.eu, 2022). Currently, the lowest mass planet detected with the radial velocity method is $GJ\,273\,\mathrm{c}$, with a mass of $1.18 \pm 0.16\,\mathrm{M}_\oplus$ (Astudillo-Defru et al., 2017)[3]. It is an Earth-like planet around a subsolar M-dwarf star, with a close orbital distance of 0.003 au. Earth-sized planets around solar-type stars are for the time being still not observable, since their gravitational pull is too weak. On the other hand, to give an example, Jupiter causes a radial velocity of the Sun of $12.5\,\mathrm{m\,s^{-1}}$. In spite of the relatively large gravitational impact of Jupiter, its detection would still be hindered due to another vital factor in most exoplanet observation methods: the orbital period of nearly 12 yr entails that the detection of just two full orbits would take 24 years. The population of RV discovered planets is thus significantly methodologically biased towards massive and short-orbit planets.

[2]The updated list of Gaia exoplanets can be found at https://www.cosmos.esa.int/web/gaia/exoplanets

[3]Lowest mass planet refers to the actual mass that was determined, not the lower mass boundary M*sin (i)

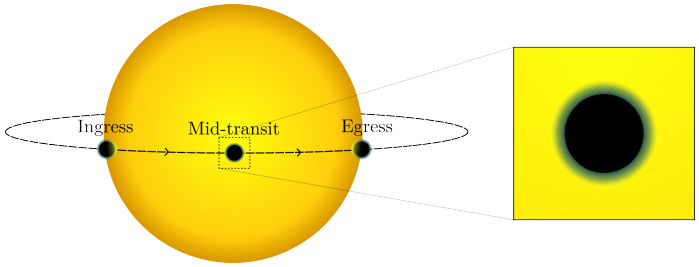

Figure 1.2: Illustration of a transit event: As the planet orbits along its path, it blocks part of the light emitted from the host star. A scale from $-\pi$ to π is used to describe the position of the planet relative to the observer and the host star, with the point of mid-transit at phase 0. The zoomed window highlights the planetary atmosphere, through which part of the stellar light is filtered. In the case of transmission spectroscopy, the light of the star is split into its spectral components. Analysis of this spectrum can give insight into the atmospheric layer around the exoplanet.

1.2.2 Transit method

In the transit method, we observe planets passing in the line-of-sight between the observer and the host star (Fig. 1.2). Because the planet obscures a part of the stellar disk, it causes a reduction in the measured flux. This called *transit depth* S and it depends on the ratio of planetary to stellar disc area,

$$S = \frac{R_p^2}{R_*^2}. \tag{1.1}$$

The transit duration is maximal for a planet crossing the centre of the stellar disc. Depending on the alignment of observer, planet and star, a transit can occur on any path across the stellar disc. Charbonneau et al. (2000) and Henry et al. (2000) simultaneously observed HD 209458 as the first transit of an exoplanet in 1999. It orbits at a distance of only 0.0475 au, ten times closer than Mercury to the Sun. Planets in close orbits are more likely to transit, because the probability p of a planet to transit across the stellar disc depends on the stellar radius R_* and on the semi-major axis a of the planetary orbit (Eq. (1.2)),

$$p = \frac{R_*}{a}. \tag{1.2}$$

Similar to the RV method, the entire population of transit discovered planets is thus significantly biased towards larger planets in close orbit. A prime example for these planets are Hot Jupiters. Since roughly 70% of exoplanets to day have been detected with this method, the bias extends to the whole detected exoplanet population. Gradually, with improving apparatus, detection of smaller planets became possible. For example, Batalha et al. (2011) detected the terrestrial planet Kepler-22 b, with a radius of roughly $1.4\,\mathrm{R}_\oplus$. Moreover, the transit method may be used to probe the exoplanetary atmosphere (Sect. 1.3).

The secondary transit (also called the secondary eclipse) can be understood as an overlap between direct and indirect imaging. The total amount of light observed by a star-planet system periodically depends on the phase of the planet. With increasing orbital phase, a higher fraction of the planetary dayside is visible to the observer. When the star eclipses the planet, the planet's contribution to the total flux will vanish, momentarily causing a drop in flux similar to the primary transit method. Comparison between the sole stellar signal and the combined signal of planet and star contains information about the planetary atmosphere. However, different parts of the planetary atmosphere are probed by the two methods: During primary transit, the day-nightside terminator is probed, and during secondary transit, the dayside is probed.

1.3 Transmission spectroscopy

If we imagine a transiting exoplanet to have an atmospheric layer above its surface, the constituents of the atmosphere may absorb light at certain wavelengths. Therefore, the signal attenuation is dependant on wavelength. Furthermore, the measured size of the transiting planet can depend on atmospheric pressure, temperature, density or compositions, and thus also be be wavelength-dependant (Seager & Sasselov, 2000). A spectrograph is used to divide the light into its spectral components. By subtracting the out-of-transit stellar spectrum from the in-transit spectrum, the light filtered through the atmosphere of the planet is isolated. With this spectral analysis, spectral signatures can then be used to reveal atmospheric constituents. Low resolution spectrography is limited to molecular bands, while with high spectral resolution analysis of atomic constituents becomes feasible. Modern high-resolution spectrographs enable unprecedented detail for transmissions spectra to enable classification of molecular bands and atomic lines. The resolution of a spectrograph is defined as $R = {}^{\delta\lambda}/_{\lambda}$, and common values for R in high-resolution spectrographs are around 100 000 (Dorn et al., 2014; Cosentino et al., 2012), and up to 190 000 for the ESPRESSO spectrograph at the Very Large Telescope (VLT) (Pepe et al., 2021).

Obtaining information about the atmospheric composition of exoplanets can give insight into the prospect of habitability and their formation history. Hot Jupiters, for example, are unlikely to have formed at close orbits around their host star (Lin et al., 1996). At these close distances, the planets can be assumed to be tidally locked due to their host star's gravitational influence. The region between the permanently irradiated day-side and the dark night-side is called the *terminator*. Because of their different irradiation, the atmospheric structure and composition may be drastically different.

Different temperatures of the two sides lead to different scale heights of the planetary atmospheres, meaning that the day-side atmosphere is more radially extended. A difference in temperature between the two sides can also lead to strong winds and jets, which in turn lead to mixing within the terminator region of the planet. Coincidentally, this implies that the planetary spectrum contains contributions from both day- and night-side. Furthermore, the highest temperature point of the day-side can be offset by jets (Showman & Guillot, 2002).

1.3.1 Exospheres

The exosphere is the highest layer of an atmosphere. Particles within the exosphere are at low density and therefore collisionless. Exposed to strong stellar radiation, particles may no longer be gravitationally bound to the planet and completely escape the atmosphere. Contents of the exosphere are sourced by lower-level atmospheric layers. In *Jeans escape*, the high end of the velocity distribution of particles in the layers below the exosphere can reach sufficiently high velocities to leave into space. Other non-thermal processes, mainly powered by solar radiation, may further cause particles to reach escape velocity (De Pater & Lissauer, 2015). As a result, the exosphere may often extend several planetary radii outwards into the interplanetary medium. Depending on the incoming solar radiation, particles may ionise on short time scales. This low-density plasma is exposed to magnetic and radiative forces and may be entrained in the solar winds, stretching far behind the object (Brace et al., 1987).

Several solar system bodies are known to have an exosphere of various compositions, including, but not limited to, hydrogen (H I) on Earth (Wallace et al., 1970), oxygen (O I) on Earth (Seki et al., 2001) and Venus (Niemann et al., 1980), and magnesium and sodium on Mercury (McClintock et al., 2009).

A number of exoplanets have been observed to feature extended exospheres. HD 209458b, a hot Jupiter close to its host star, has been observed to have extended absorption of neutral hydrogen, indicating an escaping atmosphere (Vidal-Madjar et al., 2003). Evidence for escaping neutral oxygen (OI) and ionised carbon (C II) were found subsequently (Vidal-Madjar et al., 2004). Similar to Venus, the tail morphology may resemble a cometary dust tail (Schneider et al., 1998). These findings could further be evidence for an exoplanetary magnetic field (Kislyakova et al., 2014) (see Sect. 1.4). Smaller planets at close distance may also lose material off their surface, like seen in K2 22-b (Sanchis-Ojeda et al., 2015). dos Santos et al. (2019) predicted observability of escaping hydrogen also for terrestrial exoplanets around M-dwarfs. However, due

to the strong UV-radiation, these planets may quickly deplete their atmosphere of primordial hydrogen (Hori & Ogihara, 2020; Wordsworth & Kreidberg, 2022). Such planets are therefore often thought to feature Venus-like metal-rich atmospheres. In the case of K2 22-b, not only dust, but also gasses are theorised to escape the planet, primarily sodium and ionised calcium (Ridden-Harper et al., 2019), but no significant detections of these species have been made for this planet. Another example for evaporating atmospheres is 55 Cancri e, a $2\,R_\oplus$ super-Earth in close orbit (0.0154 au) around a K-type star. Transit spectroscopy by Ridden-Harper et al. (2016) found low significance evidence for absorption of sodium and ionised calcium, potentially caused by an optically thick exosphere extending at least $5\,R_\oplus$. Extreme, mid-transit and post egress absorption of neutral hydrogen has been observed in the gas giant GJ 436 (Kulow et al., 2014), and been attributed to an extended exosphere, extending over nearly 40% of its orbit (Lavie et al., 2017).

1.4 Magnetic fields

The magnetic field of the Sun can be approximated by two different hemispheres, separated by the heliospheric current sheet (De Pater & Lissauer, 2015). The stellar wind carries the magnetic field of the Sun outwards. Close to the star, the protons move at sub-sonic speeds, but accelerate to super-sonic velocities further away. Due to the rotation of the Sun and the acceleration of stellar wind protons, the heliospheric current sheet takes on a spiral structure known as the *Parker spiral*. Because of this spiral structure, the direction of the stellar magnetic field in the co-rotating reference frame of the planet may not be parallel to the planetary motion. This depends on the orbital distance of the planet to its star. A magnetic field can be intrinsic to a planet, but can also be induced through interactions between the stellar wind and ionised particles in the atmosphere. This induced magnetic field acts similar to an intrinsic magnetic field, creating a vacuity in the stellar wind, which divides the stellar magnetic field and "protects" the planet from direct exposure to stellar wind (De Pater & Lissauer, 2015). In presence of an internal magnetic field, this cavity is called the *magnetosphere*. For an induced magnetic field, we speak of an *ionosphere*[4]. Beyond a certain distance, the stellar and magnetic field lines reconnect. The stretched out planetary magnetic field away from the star is called the *magnetotail*. Interactions between a planetary magnetic field and super-sonic stellar wind particles forms a bow shock, in which the protons are quickly decelerated. For both gas giants and terrestrial planets, escaping ions are affected by magnetic fields. Stellar magnetic field, planetary magnetic field and stellar wind alter the morphology of the tail, as well as acceleration of ions within it (García Muñoz et al., 2021). In turn, this can then affect absorption features in transmission spectroscopy. Loyd et al. (2023) give estimates to the planetary magnetic field of GJ 436 b through measurements of the variation of the host star in the UV. They argue that interactions between the planetary magnetic field and the star could cause weak solar flares, but the results are not strong enough to be significant. For HD 209458 b, Kislyakova et al. (2014) modelled the planet with a static magnetic field in order to match observations of escaping neutral hydrogen. Ben-Jaffel et al. (2022) try a more complex approach for the super-Earth HAT-P-11 b in order to estimate the planetary magnetic field. They simulate different layers of the atmosphere and the interplanetary medium with different codes, in order to match observational results of neutral hydrogen and ionised carbon. While these are indications for detections of the effects of magnetic field of exoplanets, the complex interactions between various components within stellar systems have not been explored well enough to conclusively confirm the existence of them.

1.5 Close-orbit terrestrial exoplanets

Terrestrial exoplanets in close orbits are a highly variable class of planets. These include rocky planets with and without an atmosphere, lava worlds and ocean worlds. With the Hubble Space Telescope (HST), transit observation of these smaller planets can investigate their atmosphere in the UV, optical and Infrared (IR).

[4]Bodies with an internal magnetic field still have an ionosphere as part of their atmosphere, in which particles are ionised by stellar radiation.

The previously mentioned super-Earth 55 Cancri e is expected to have a surface temperature $> 2000\,\mathrm{K}$. It has been shown to have signatures of a carbon-rich atmosphere (Tsiaras et al., 2016). Transmission spectra obtained for the planet HD 97658 b using HST (Knutson et al., 2014) suggest an atmosphere either dominated by clouds, preventing water detection, or one with high metallicity. In the case of the Trappist planets, hydrogen-rich cloud-free scenarios are unlikely (e.g. de Wit et al., 2016). Recent results from the JWST furthermore suggest that Trappist 1-b features no atmosphere at all, due to its proximity around the strong UV-emitting M-dwarf host star (Greene et al., 2023). A high molecular weight atmosphere is also a likely scenario for the $2.7\,\mathrm{R}_\oplus$ GJ 1214 b, which features no absorption in the IR for observations using HST (Berta et al., 2012). High-altitude clouds may also be the reason for these observations. Mugnai et al. (2021) investigated the $1.13\,\mathrm{R}_\oplus$ super-Earth GJ 1132 b using model fitting of data obtained by HST. Non-detection of molecular IR absorption bands indicate different possible scenarios, including a cloudy hydrogen-dominated atmosphere, or a tenuous, non-detectable atmosphere. Distinguishing between the different scenarios is not yet possible for the narrow-band HST data.

1.6 Planet π Men c

pi Men (also π Men) is a solar G0V-type star, visible to the naked eye (Gandolfi et al., 2018). Three companion planets have been confirmed (Jones et al., 2002; Gandolfi et al., 2018; Huang et al., 2018). Pi men c is the innermost of those planets, with an orbital distance of 0.06 au (Tab. 1.1). As a result, the planet is assumed to be tidally locked and its orbit to be circularised, i.e. at 0 eccentricity. For the same reason it also is subject to strong stellar irradiation, up to 2000 times that of the Earth in the Extreme Ultraviolet (XUV) (King et al., 2019). Previous studies of its atmosphere document missing absorption in the Ly α, indicating no or low atmospheric abundance of atomic or molecular hydrogen, and higher abundance of heavier molecules, such as CO_2 or H_2O (García Muñoz et al., 2020; King et al., 2019). This is in accordance to previous research, as discussed in Sect. 1.3.1.

García Muñoz et al. (2021) obtained transmission spectra of π Men c in the far UV with the HST. Covering stellar lines of abundant elements like hydrogen, carbon and oxygen, they report significant absorption from a C II-triplet around 1335 Å up to $6.76 \pm 0.02\,\%$. The triplet consists two close lines at 1335.66 Å and 1335.71 Å, respectively, and a third line at 1334.53 Å. Because of absorption by the Interstellar Medium (ISM), a decrease in flux was only observed for the upper two lines. From the lifetime of the planet, together with the non-detection of hydrogen, they infer a high-metallicity atmosphere, abundant in carbon. Excess absorption in the C-II lines could then be caused by ions within an extended exosphere, beyond the planet and towards the observer. This theory goes in line with the proximity of the planet to the Fulton gap: planets around this radius can either hold on to their envelope or lose it, leading to an observed bimodality in the radius distribution Owen & Wu (2017). This indicates that mass loss of π Men c could continue for several Gyr. Their photochemical-hydrodynamic model indicates that ion densities in the source regions cannot exceed $1 \times 10^6\,\mathrm{cm}^{-3}$. García Muñoz et al. model the exosphere of π Men c using an approximate size of the exosphere of 15 planetary radii and a 1D atmospheric model. They take several chemical processes into account, and use ion velocities from hydrodynamic predictions. Planetary particles are accelerated away from the planet by the stellar wind. Furthermore, they consider photo-ionisation of C II to C III, but question the importance of collisional ionisation. With this, they are able to put a lower limit on the mass loss rate. Additionally, they mention that 3D modelling with the inclusion of magnetic forces will advance the efforts of exosphere research.

π Men c therefore is a prime candidate for further research on escaping exospheres in terrestrial exoplanets. We follow up on the suggested research of Earth-like exoplanets to constrain mass loss rates of π Men c. Doing this, we hope to aid the investigation on the atmospheric composition of π Men c in particular, but other terrestrial exoplanets in general. Furthermore, we evaluate the importance of magnetic forces in exoplanet modelling. By predicting the spectra of exospheres, follow-ups on simulations with observations could help verify theories on extraterrestrial magnetic fields, exospheric escape and exoplanet evolution. Additionally, new observations of previously overlooked species could be predicted.

Table 1.1: Parameters of the pi Men system, taken from Damasso et al. (2020).

pi Men	
Stellar mass	$1.07 \pm 0.04\,\mathrm{M}_\odot$
Stellar radius	$1.17 \pm 0.02\,\mathrm{R}_\odot$
$\mathbf{T}_{\mathrm{eff}}$	$5998 \pm 62\,\mathrm{K}$
Age	$3.92^{+1.03}_{-0.98}\mathrm{Gyr}$

pi Men c	
Mass	$4.3 \pm 0.7\,\mathrm{M}_\oplus$
Radius	$2.11 \pm 0.05\,\mathrm{R}_\oplus$
Semi-major axis	$0.0680 \pm 0.0008\,\mathrm{au}$

Chapter 2

Theory and Methodology

In this chapter, we discuss the methods used to model the transmission spectra of exoplanet atmospheres. We first introduce the code that was used to produce the three-dimensional models of planet and exosphere in Sect. 2.1. An introduction to the theory of radiative transfer can be found in Sect. 2.2.1. Subsequently, we present two radiative transfer codes, and their respective advantages and disadvantages. Details on the absorption line shape and position are discussed in Sect. 2.2.4. A synopsis about the impact of the stellar spectrum is in Sect. 2.2.7. As a proof of concept, we present results from the fiducial run in Sect. 2.4.

2.1 Plasma model: AMITIS

All plasma models used in this work were provided by Shahab Fatemi and computed using the hybrid-kinetic code Advanced Modelling Infrastructure in Space Simulations (AMITIS) by Fatemi et al. (2017). Even though AMITIS has been developed for the modelling of solar system objects like Mercury (Fatemi et al., 2020), Ganymede (Fatemi et al., 2022) and asteroids (Fatemi & Poppe, 2018), it has not been used in exoplanet research before. AMITIS includes physical processes like magnetic fields, electron pressure or stellar wind pressure to compute the time-dependant evolution of a system. Ions are considered kinetic particles and electrons a massless, negatively-charged fluid, which is called the hybrid approach. Hence, the net plasma charge density is zero. The description of the flow field is Eulerian. Magnetic and electric fields and their forces on ions and electrons are calculated by solving approximations of Maxwell's laws and the position and momentum of charged particles. The electric field is calculated by a generalisation of Ohm's law, and the magnetic field is evaluated using Faraday's law (Fatemi et al., 2017). Ions are only affected by electromagnetic forces and do not interact with each other, so that

$$\frac{\mathrm{d}\mathbf{r}_i}{\mathrm{d}t} = \mathbf{v}_i, \qquad \frac{\mathrm{d}\mathbf{v}_i}{\mathrm{d}t} = \frac{q_i}{m_i}(\mathbf{E} + \mathbf{v}_i \times \mathbf{B}), \tag{2.1}$$

for a particle of mass m_i and charge q_i, position $\mathbf{r}_i$ and velocity $\mathbf{v}_i$ and the electric field $\mathbf{E}$ and magnetic field $\mathbf{B}$ (Fatemi et al., 2017). Altogether, this yields a six-dimensional model in position- and velocity-space. In the context of this work, AMITIS is used to model the interactions between the stellar wind, the stellar magnetic field, exoplanetary atmospheres and exoplanetary magnetic fields. In AMITIS, a model with initial parameters is set up and evolved. Ions continuously generated within a defined region around the planet, with defined scale heights for different species. The simulation timestep depends on the grid size as well as on some of the simulation parameters. In our case, a typical timestep of 5 ms is used. For the steady state, simulation results are checked with earlier times (≈100 s difference). If no noticeable differences are visible, it is considered the final solution. This yields a snapshot of the three-dimensional simulation, which is then further processed in radiative transfer codes (see Sect. 2.2). This snapshot includes grid-based information about species-wise particle- and charge-densities, and also velocity information in three spatial dimensions

for tracer particles of these species. The stellar parameter options include, but are not limited to, electron and proton density and velocity, stellar magnetic field strength and orientation, and stellar gravity. It is important to note that the star is not actually modelled, but only its magnetic (and gravitational) field and the stellar wind in the interplanetary space. For the non-stellar object, in our case a terrestrial-sized planet, parameters include ion type, particle source regions and rates, planetary size and mass, magnetic field strength and orientation. An example AMITIS simulation set-up is shown in Fig. 2.1.

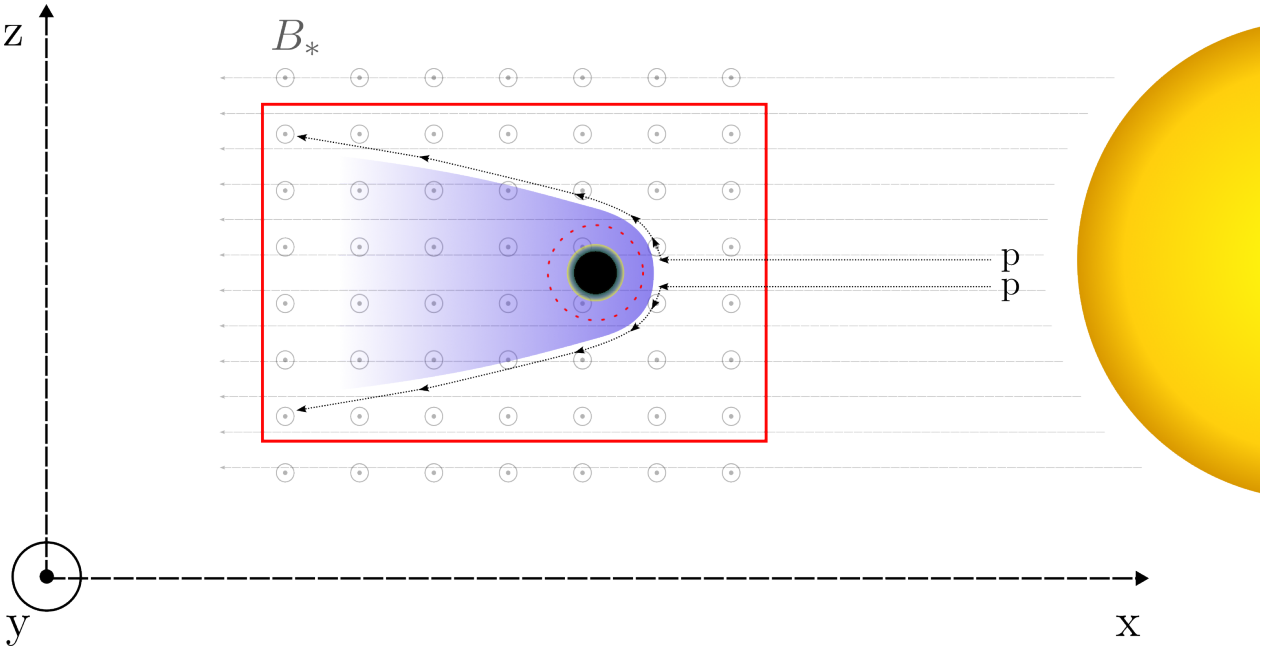

Figure 2.1: Visualisation of the simulation environment (not to scale). The AMITIS simulation box is surrounded by a red rectangle. Within that, the planetary exosphere is shown in blue, and a red dashed circle marks the source region for one type of particle. Different particles may have different source region sizes. The stellar magnetic field and planetary movement are in positive y-direction. Example paths of stellar wind protons are shown with black dashed lines. Ions tails are shown in blue, forming tails behind the planet. The tails are considered part of the exosphere clear distinction or distance at which we make a distinction between the exosphere and the tails.

Research on exoplanet magnetic fields has been done for hot Jupiters (Loyd et al., 2023; Kislyakova et al., 2014), as the effects of evaporating exospheres are more prominent for larger planets. As a result from its intended use in solar system research, the possible planetary size has a soft upper cap. This is due to the limitation of computational resources at this time. Models are therefore limited to terrestrial planets, up to sizes of several $R_\oplus$. This thesis extends the work on terrestrial exoplanet magnetic fields.

2.1.1 Atmospheric model

A classical model for the source region begins with a spherical shape, and density decreasing with altitude. This follows from hydrostatic equilibrium, and is an approximation of the more complicated atmospheric structure of planets. In AMITIS, the rate of ion production not only depends on vertical height, but also on the zenith angle, which is the angle between the normal of the planet surface and the star. In practise, that means that ionisation probability decreases when photons have to penetrate through more atmospheric mass. Chapman (1931) defined a function that gives ionisation fractions dependant on zenith angle and density profile. Together with a density profile of the atmosphere ionisation rates for particles are calculated. Since

the density profiles of atmospheric particles are different, so are their source rates and locations.

2.2 Radiative transfer

Radiative transfer is the simulation of absorption, scattering and emission of light passing through a medium. The attenuation depends on the constituents of the medium. Each molecule or atom has a set of transitions, where atomic electron configurations change. Transitions are associated with a change in energy, and photons with that specific energy may be emitted or absorbed. In a transmission spectrum, absorption features are therefore attributed to individual transitions of individual species. Molecules usually absorb in bands, i.e. absorption over a range of wavelengths, and atoms / ions in lines (Sharp & Burrows, 2007, table 1). The strength of absorption features may further depend on absorber density, temperature, transition constants, while the wavelength of absorption depends on particle velocity.

To model the transmission spectrum of exoplanets, we use the output of the AMITIS code, which contains most of the necessary information, specifically species densities and line-of-sight-velocities. For all simulations, the planet is assumed to be mid-transit, i.e. directly in front of its host star. Similar to atmospheric absorption, the exosphere causes flux reduction for lines of the ionised species. Two different codes were then used to create synthetic transmission spectra. To explain radiative transfer, we introduce the theory in Sect. 2.2.1.

2.2.1 Atomic theory

The theoretic background is largely taken from Draine (2011). For atoms, transitions between electron shells and their associated energies are quantised. The absorption of energy E carried by a photon at wavelength γ can excite an atom X, raising an electron from a lower level l to an upper level u,

$$X_l + E_\gamma = X_u, \tag{2.2}$$

where the energy difference between the two levels is equal to the photon energy. Hence, the probability of absorption depends both on the number density of the absorbers n_l as well as on the spectral energy density at a specific wavelength $u(\nu)$,

$$\left(\frac{\mathrm{d}n_l}{\mathrm{d}t}\right)_{l\to u} = n_l B_{lu} u(\nu) \tag{2.3}$$

with the Einstein coefficient B_{lu} as the proportionality factor for this transition. Deexcitation from the higher energy state can occur through spontaneous emission and stimulated emission. Spontaneous emission is a stochastic process, independant from the surrounding radiation field,

$$X_u \to X_l + E_\gamma. \tag{2.4}$$

In an equilibrium between excitation and deexcitation, both levels are populated according to their energy difference. The stochastic deexcitation process is defined by the Einstein coefficient A, which is related to B_{lu} by

$$B_{lu} = \frac{g_u}{g_l}\frac{c^3}{8\pi h\nu^3}A_{ul}, \tag{2.5}$$

where g_u and g_l are the multiplicities of the levels. Both absorption and spontaneous emission are fully determined by A_{ul}. When ignoring scattering, the wavelength-dependant absorption of radiation passing through a medium composed of a single absorber can be calculated using Beer-Lamberts law[1],

$$I(\nu) = I_0 e^{-\tau}. \tag{2.6}$$

The flux I measured behind the absorber is equal to the initial flux I_0 attenuated exponentially by the

[1] We omit scattering and stimulated emission

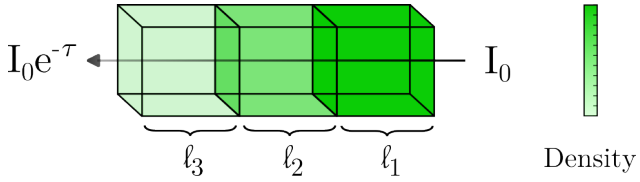

Figure 2.2: Attenuation by different particle densities. The total optical depth is the sum of the optical depths in each compartment i, given by $\tau_i = n_i l_i \sigma$

optical depth τ. Higher optical depth means more absorption. Moreover, τ is defined as the integral

$$\tau = \int_0^l \sigma n(s) \mathrm{d}s, \tag{2.7}$$

where $\sigma(s)$ is the *absorption cross section* of the absorber and $n(s)$ the number density along of the absorber along the path of light. For a medium of constant number density and absorption cross section, this simplifies to $\tau = \sigma N$, with the *column density* of the absorber $N = ln$. As an approximation for numerical calculations, in multiple discrete absorbing compartments (see Fig. 2.2), the total optical depth is the sum of the individual optical depths, i.e.

$$\tau_{\mathrm{tot}} = \sum_i \tau_i = \sigma \sum_i n_i l_i, \tag{2.8}$$

where we assume a single absorber, and constant σ. We will see later that the absorption cross section may also be dependant on the location, so that

$$\tau_{\mathrm{tot}} = \sum_i \tau_i = \sum_i \sigma_i n_i l_i. \tag{2.9}$$

2.2.1.1 Atomic line theory

Draine (2011) define the intrinsic line profile ϕ_ν of a single transition as

$$\phi_\nu^{\mathrm{intr}} = \frac{4\gamma_{ul}}{16\pi^2 \left[\nu - (1 - {}^{v}/_{c})\nu_{ul}\right]^2 + \gamma_{ul}^2}, \tag{2.10}$$

where ν is the frequency, γ_{ul} the intrinsic line width, as the sum of all Einstein A_{ul} coefficients to the energy level[2], c the speed of light and ν_{ul} the intrinsic line centre. Convolving the intrinsic line profile with the velocity distribution of the absorber gives the line profile

$$\phi_\nu = \int p_v(v) \frac{4\gamma_{ul}}{16\pi^2 \left[\nu - (1 - {}^{v}/_{c})\nu_{ul}\right]^2 + \gamma_{ul}^2} \mathrm{d}v, \tag{2.11}$$

with $p_v \mathrm{d}v$ the probability of finding the absorber moving with velocity in the interval between v and $v + \mathrm{d}v$ (Draine, 2011, Ch. 6, p. 59, Eq. 6.36). Using discrete velocities i, the integral becomes a sum, so that

$$\phi_\nu = \sum_i p_v(v_i) \frac{4\gamma_{ul}}{16\pi^2 \left[\nu - (1 - {}^{v_i}/_{c})\nu_{ul}\right]^2 + \gamma_{ul}^2} \Delta v_i, \tag{2.12}$$

Within each cell of the AMITIS simulation, we can obtain an approximate distribution of velocities by creating a normalised histogram of velocities of tracer particles. The absorption cross section and the line profile are related by (Draine, 2011, Eq. 6.24)

$$\sigma(\nu) = \frac{\pi e^2}{m_e c} f \phi_\nu = \frac{\pi e^2}{m_e c} f \sum_i p_v(v_i) \frac{4\gamma_{ul}}{16\pi^2 \left[\nu - (1 - {}^{v_i}/_{c})\nu_{ul}\right]^2 + \gamma_{ul}^2} \Delta v_i, \tag{2.13}$$

[2]We only consider ground state transitions, and thus for each transitions $\gamma_{ul} = A_{ul}$.

where m_e is the mass of the electron, e is the charge of the electron in electrostatic units[3], and f the dimensionless oscillator strength. We consider multiple transitions t of an absorber,

$$\sigma(\nu) = \sum_t \frac{\pi e^2}{m_e c} f_t \sum_i p_v \Delta v_i \, \frac{4\gamma_t}{16\pi^2 \left[\nu - (1 - {}^{v_i}/_c)\nu_t\right]^2 + \gamma_t^2}, \tag{2.14}$$

where we denote dependancy of oscillator strength f_{ul}, line centre ν_{ul} and intrinsic width $\gamma_{ul} = A_{ul}$ on the transition with a subscript t, while also dropping the energy level notation (therefore, $f_{ul} = f_t$, $\nu_{ul} = \nu_t$ and $\sigma_{ul} = \sigma_t$). Using Eq. (2.9) we further relate the absorption cross section to optical depth. Voxels have equal side length Δx in radial direction l in AMITIS, so summing over all voxels (cells c) in a single column

$$\tau(\nu) = \sum_{\mathrm{c}} \sum_t n_c l \frac{\pi e^2}{m_e c} f_{st} \sum_i p_v \Delta v_i \, \frac{4\gamma_t}{16\pi^2 \left[\nu - (1 - {}^{v_i}/_c)\nu_t\right]^2 + \gamma_t^2}. \tag{2.15}$$

N_c is the particle surface density in cell c. From AMITIS, we calculate $N_c = N_\rho \Delta x$, where N_ρ is the particle volume density. With multiple absorbers (species s), we obtain

$$\tau(\nu) = \sum_s \sum_{\mathrm{c}} n_{sc} l \sum_t \frac{\pi e^2}{m_e c} f_{st} \sum_i p_v \Delta v_i \, \frac{4\gamma_t}{16\pi^2 \left[\nu - (1 - {}^{v_i}/_c)\nu_t\right]^2 + \gamma_t^2}. \tag{2.16}$$

Species dependancies are denoted with a subscript s. Particle density N_{sc} then also depends on species. For the oscillator strength, dependancy on both species and transition is redundant, since transitions are inherent to species, but it is left in for clarity. We show a list of atomic lines in the appendix.

2.2.1.2 Relative flux absorption

Finally, the absorption in each column m is calculated with Eq. (2.6),

$$I_m(\nu) = I_0 e^{-\tau_m(\nu)}, \tag{2.17}$$

where we assume a uniform incident stellar continuum flux $I_0(\nu) = I_0$. From this, we calculate the specific attenuation at frequency ν for each column in our box. Suppose a total of M columns with non-zero τ. We do not calculate radiative transfer through the planetary interior. The planet is assumed opaque at all wavelengths, and blocks a fraction of the flux equal to ${}^{R_P^2}/_{R_*^2}$,

$$\frac{I(\nu)}{I_0} = \frac{I_0(R_*^2 - R_P^2)}{I_0 R_*^2} = 1 - \frac{R_P^2}{R_*^2}, \tag{2.18}$$

with R_P the planetary and R_* the stellar radius. From the total flux, we subtract all columns with non-zero optical depth, and add the reduced flux by those columns from Eq. (2.17),

$$\frac{I(\nu)}{I_0} = \frac{R_*^2 - M\Delta y \Delta z + \sum_M \Delta y \Delta z \, e^{-\tau_m(\nu)}}{R_*^2} = 1 - \frac{A_{\mathrm{col}}}{R_*^2} \left[M - \sum_M e^{-\tau_m(\nu)} \right]. \tag{2.19}$$

All columns share Δy amd Δz, and we set $\Delta y \Delta z = A_{\mathrm{col}}$. Combining both the planetary and exospheric attenuation, we add Eq. (2.18) and Eq. (2.19) into

$$\frac{I(\nu)}{I_0} = 1 - \frac{R_P^2}{R_*^2} - \frac{A_{\mathrm{col}}}{R_*^2} \left[M - \sum_M e^{-\tau_m(\nu)} \right]. \tag{2.20}$$

Fig. 2.3 visualizes the implementation of Eq. (2.6) and Eq. (2.20) in Plasmetheus.

[3]It is important to use ESU units for e, so that f is dimensionless.

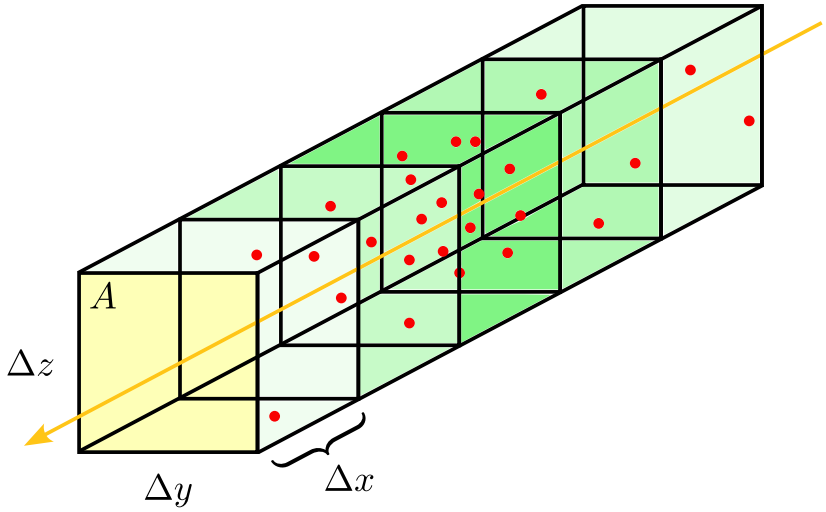

Figure 2.3: Single column in Plasmetheus. From AMITIS, we get information about the voxel-wise particle densities (shown as green) and tracer particle velocities (shown in red). The column has an area $A = \Delta y \Delta z$. Radiation at wavelength λ is attenuated according to Eq. (2.6).

2.2.2 Line list

All line list data is taken from NIST Atomic Spectra Database (Kramida et al., 2022). We show all lines from the selected species C II, Mg II and O II in appendix Tab. 1. These were shown due their their previous relevance in exospheres (García Muñoz et al., 2021; McClintock et al., 2009; Vidal-Madjar et al., 2013; Niemann et al., 1980). Within this list, only lines with high oscillator strength are selected for spectra modelling, since these are the lines with visibly significant absorption. We limit our selection to ground state transitions, because these are the ones we are currently able to model.

2.2.3 Prometheus

Initially, we used PRObing Mass loss in Exoplanetary Transits with Hydrostatic, Evaporative and User-defined Scenarios (Prometheus), which was developed by Andrea Gebek (Gebek & Oza, 2020). Prometheus uses atmospheric density profile to do radiative transfer for exoplanets. It calculates synthetic absorption spectra. In order to use it, we coupled the three-dimensional density information from the AMITIS file to PROMETHEUS. The code builds a cylindrical coordinate system, with the longitudinal axis (chord) along the line-of-sight of the observer. At the centre of the systems sits the planet. For the wavelength grid, any range between 500 Å to 55 000 Å can be selected, and a constant continuum stellar flux is assumed for all wavelengths. Density information is then taken from an interpolated AMITIS grid. Since Prometheus was developed for atmospheric simulations, where densities are high enough for collisional interactions, the distributions of velocities in each cell is assumed to be Gaussian[4]. Even when disregarding the incorrect assumption of Gaussian-distributed velocities, associated standard deviations are not included in the AMITIS field. Therefore, the σ_v is set to $1\,\mathrm{cm\,s^{-1}}$ per default in Prometheus. To discuss the drawback of assuming Gaussian velocity distributions, we explain the details of the line profile in the following section.

2.2.4 Line profile and position

The intrinsic line profile described in Eq. (2.10) is given by a Lorentz profile. While dealing with only ground-state transitions, the lower energy state is at zero, and thus the Full Width at Half Maximum (FWHM) of

[4]Then, from Eq. (2.11), the mathematical theory changes slightly, and is not further explained here.

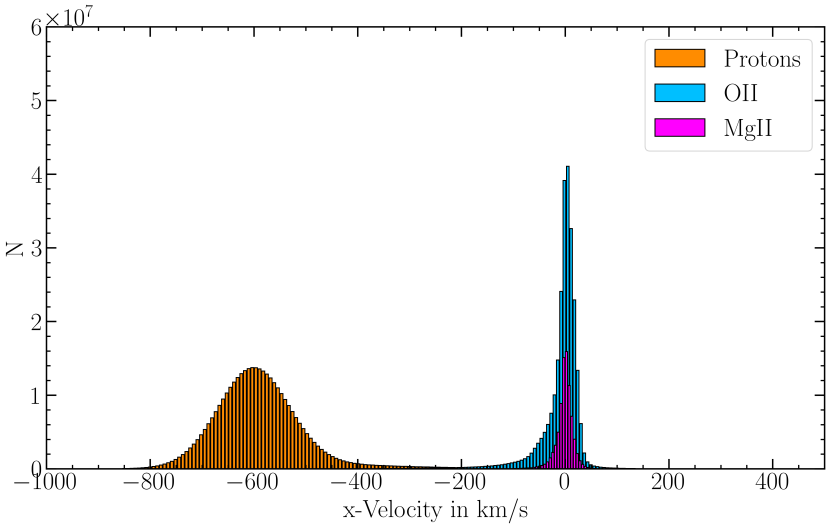

Figure 2.4: Distribution of tracer particle velocities in the fiducial run of AMITIS. Protons have high absolute mean velocity. The heavier species Mg II and O II are centred around 0 and have asymmetric tails. Negative velocities of these species are due to entrainment and acceleration in the stellar wind.

the intrinsic line profile can be derived to

$$\mathrm{FWHM} = \frac{\gamma_{ul}}{2\pi} = \frac{A_{ul}}{2\pi}. \tag{2.21}$$

Subsequently, the line profile can be changed by various effects. First and foremost, the line profile can be broadened through the thermal motions of the absorber. In Prometheus, this is implemented as a convolution with a Gaussian, yielding a Voigt profile. This assumption holds true for collisional regimes, but not generally for exospheres, where particle densities are low. Second, movement of the absorber changes the centre of the line (Eq. (2.10)). In the case of exoplanets, movement due to relative motion between the observer and the absorber (bulk movement) is larger than thermal motion. This can be seen in Fig. 2.4, where we show the distribution of tracer particles' radial velocities in the fiducial run of AMITIS. Protons, due to their lower mass, and because they are not sourced at the planet, have a significantly higher absolute mean velocity, seen as a Gaussian distribution centered around $-600\,\mathrm{km\,s^{-1}}$. Heavier species show a different, non-Gaussian distribution of velocities, centred around zero. The assumption of Gaussian velocities is therefore not valid. Their centre around $0\,\mathrm{km\,s^{-1}}$ can be explained by the low initial velocities these particles posses before being entrained in the stellar wind. Furthermore, the tails of these species show asymmetries, with longer tails extending to high negative velocities. These are the particles entrained in and accelerated by the stellar wind. Particles with positive line-of-sight velocities stream towards the host star, likely due to interactions within the ionosphere. The residual thermal motion alone of these particles is not large enough to explain the observed velocities. Not all velocities present in a simulation will contribute to its transmission spectrum, as particles either in front or behind of the planet relative to the host star and the observer are obstructed and thus not visible. For later simulations most particles are not obstructed by the planet due to the extent of the exosphere.

In transmission spectroscopy, the orbital radial velocity of the planet induces a shift in the spectrum. From ingress until transit-midpoint, the signal is blueshifted, and from mid-point until egress, it is redshifted. This bulk radial velocity does not influence line shape, but its position. As of now, we only calculate the transit-midpoint, where both stellar and planetary radial velocity are zero.

2.2.5 Plasmetheus

The second code used is self-written, but partly reuses elements and structure from Prometheus. It specifically only uses AMITIS output data to calculate synthetic transmission spectra. The significant advantage over Prometheus is the ability to include non-Gaussian velocity distributions. In fact, this is especially important with space plasma. Radial velocities of neither large- nor small-scale structures within the exosphere are well approximated by Gaussian distributions, for species other than ionised Hydrogen (Fig. 2.4). Including the information about the velocities of particles is vital, since the observed spectrum may be red- or blue-shifted, depending on the movement of the particles. In Plasmetheus, instead of assuming a Maxwellian distribution for the radial velocity of particles, we instead take the velocity distribution of tracer particles directly from the model, to use in Eq. (2.16). While each tracer particle in itself represent a larger number of particles (1 macro particle $\approx 10^{24}$ actual particles), and therefore would have a velocity distribution itself, the effect of thermal line broadening from this is small compared to the line broadening of bulk velocities of tracer particles. We expect the error of the tracer particle velocity distribution to be small. The effect of variations in the assumed velocity spread within each tracer particle is partially covered by artificial line width increase, as explained in Sect. 2.2.6, and therefore negligible here.

2.2.6 Spectral resolution and sampling

The resolution of a spectrograph is defined as

$$R = \frac{\lambda}{\Delta\lambda} = \frac{c}{\Delta v}. \tag{2.22}$$

The resolution of a spectrograph can directly by converted into the minimum change in velocity detectable. With an example value of $R = 100000$, at 1000 Å, details with a minimum width of 0.01 Å would be resolved, or $3\,\mathrm{km\,s^{-1}}$. When a real spectrograph samples the signal, this is roughly equivalent to a convolution with the original spectrum. Without any changes the spectra produced by Plasmetheus are uneven (Fig. 2.5). This is due to narrow intrinsic line width of the transitions, located at specific velocities of the tracer particles. Such spikes are not only unphysical, but also would not be visible with a spectrograph due to the aforementioned convolution.

In order to avoid this, we can change the intrinsic line width. We can choose different values lower than the dispersion corresponding to $3\,\mathrm{km\,s^{-1}}$ visible with a spectrograph. This results in a smoother synthetic spectrum. For appropriate values, this does not change the line shape or absorption depth of the peaks (Fig. 2.5).

We argue that the smoothed spectrum may more closely represent the true spectrum of the exospheric plasma obtained by a spectrograph. The sharp edges in transit depth of the original spectrum are unphysical, as the discrete values for tracer velocities do take into account the spectrum of velocities that each tracer particle represents. Artificially increasing the intrinsic line width partially accounts for thermal smoothing of the absorption line. Spectral details are not smeared significantly by this process. This approximation is therefore assumed correct for the scope of this thesis.

2.2.7 Stellar spectrum

Usually, we assume a constant, nonzero continuum stellar flux for our radiative transfer codes. For the results produced in radiative transfer, we divide by the stellar spectrum to isolate the atmospheric component. This normalises our spectrum and gives us the relative decrease in flux (Fig. 2.5). This assumption usually holds true for the optical and infrared spectrum. In order to obtain information about the stellar spectrum of π Men, we can compare it to the star HD 209458. This is also a solar G0V-type star, slightly older than π Men. We presume that the continuum flux of solar-type stars declines in the UV. Both HD 209458 and π Men are younger than the Sun, implying a higher UV flux than our present-day sun. For lower UV flux, higher SNR is necessary to observe extinction from exoplanetary ions. From near to far UV, the flux may

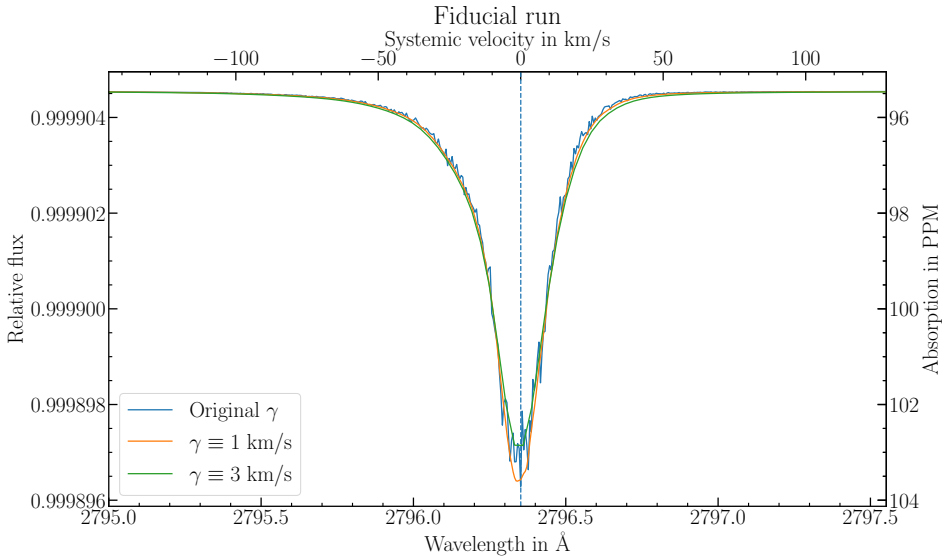

Figure 2.5: Proof of concept of artificially increasing the intrinsic line width of transition lines, shown for the fiducial run and the Mg II line at 2796.352 Å. With original γ, the unevenness in the absorption line is caused by the discrete distribution of tracer particle velocities in the AMITIS model and the small intrinsic line width. With γ increased to line width corresponding to $1\,\mathrm{km\,s^{-1}}$ at the specific line centre, the overall profile remains, but is well sampled. The average velocity of Mg II tracer particles is $-1.756\,\mathrm{km\,s^{-1}}$, which reflects in the smoothed line as a minimal negative offset of the line peak. For the original curve, this detail is lost. Increasing γ further leads to a broadening of the line. This effect is undesired and leads to wrong results. We therefore cap γ at $1\,\mathrm{km\,s^{-1}}$ relative to the centre of the line. The offset of the spectral peak can be difficult to observe when taking Signal-to-noise ratio (SNR) of UV spectrographs at transit depth of several percent into account.

decrease by orders of magnitude. In the far UV atomic emission lines of (ionised) species dominate the stellar spectrum. Changes in the stellar spectrum due to Doppler shifts induced by the planet are small. On the other hand, the change in orbital velocity for the planet is large. Over the course of the transit, the static atomic UV emission features in the stellar spectrum could be used to scan the shifting planetary absorption lines. Furthermore, strong redshift features caused by exospheric extinction may even persist for some time post-egress, in the case of an extended exosphere trailing the planet. Knowing the orbital velocities of both the star and the planet, this may allow to set constraints for the extent of the planetary ion tail. Within the scope of this work, we keep the assumption of a non-zero continuum stellar flux, but future work would benefit from including real stellar spectra. This is especially important for ingress and egress spectroscopy, and to correctly predict the noise levels of spectra in the UV. In the optical, the stellar continuum flux is higher, and certain ionised species also have lines there. High resolution spectrographs, even ground based ones, could be used in this field of research.

2.3 Parker Spirals

Particles sourced from the planet are affected by the magnetic field. Consequently, the shape of the exospheric cloud, and furthermore its optical depth, depends on the direction of the stellar magnetic field. We therefore need to take the orientation of the stellar magnetic field into account when running AMITIS plasma models. The parameters of the Parker spiral, as the heliospheric current sheet, depends on the proximity to the star and the velocity of the stellar wind (Sect. 1.4). For planets in close orbit around their host star, Parker

spirals can lead to an angled magnetic field orientation. As a consequence, this can affect interactions between the ionosphere, exosphere, stellar wind and planetary magnetic field. In order to account for the possible subsequent effects, the orientation of the stellar magnetic field can be altered in AMITIS. Doing this, we can investigate the importance of Parker spirals for synthetic transmission spectra modelling in (exo-)planetary magnetic field environments. In addition, the direction of the incoming stellar wind protons may also have a component in negative y-direction Fig. 2.1, due to the orbital movement of the planet around the star. We account for this in all simulations of π Men c.

2.4 Fiducial run

The fiducial model from the AMITIS code is an Earth-like planet, both in size and magnetic field strength. For parameters, we used box side lengths of $x = 116.4 \times 10^3$ km, $y = 252 \times 10^3$ km and $z = 324 \times 10^3$ km, and a planet of radius of 6800 km, placed at the centre of the box (Fig. 2.6). Stellar size is set to $1\,R_\odot$, and solar wind particles travel (from the right) with a density of roughly $40\,cm^{-3}$. This is a typical reference value for the stellar wind density at Mercury's orbit[5]. Besides protons, ionised oxygen and ionised magnesium were included. The protons interact with the planetary atmosphere and magnetic field, resulting in the formation a bow shock, seen as a sharp jump in proton density. Within the front region of the bow shock, the average proton density is $94\,cm^{-3}$, about twice as high as in the stellar wind. Just below the bow shock, closer to the surface, the proton density drops down, where the source regions of ionised oxygen and magnesium set it. Directly above the planetary surface, no protons can be found, and the particle density is dominated by oxygen and magnesium, with particle densities up to $1000\,cm^{-3}$. For all three species, the escaping exosphere extends in a cone-like shape behind the planet. On the planetary night-side, the proton density is as high as in the bow shock, but densities of O II and Mg II are significantly lower than on the day-side. Interactions between the magnetic fields and the ions create regions without particles, seen as wings above and below the line-of-sight between observer and planet. These regions are more pronounced for protons than for the other two particles. As the proton bow shock broadens and expands behind the planet, proton densities decrease back to stellar wind level. In transit, regions in front and behind the planet are blocked by the planet. For a non-bend tail morphology, this prohibits detection of parts of the high density day side region, as well as the thin trail behind the planet. Column densities as seen by an observer are shown in Fig. 2.7. Blocked columns are marked with a black circle. Proton densities are high all-throughout, but have a ring-like morphology around the planet. The low column density in the middle is due to the previously mentioned magnetic field effect on charged particles, which becomes more apparent when inspecting the column density. On the other hand, column densities for O II and Mg II increase monotonically towards the planet, because the particles are sourced close around the surface. Despite the high column densities of protons, they are not of interest for us at the moment, since they have no absorption lines. For models which include charge exchange, recombination or other processes of forming neutral hydrogen, extended absorption in the Lyα line may become visible in the tail, as discussed in Sect. 1.3.1. Meanwhile, we focus on the heavier species. As a proof of concept, a synthetic spectrum of the fiducial run was calculated using PROMETHEUS, and is shown in Fig. 2.8. Between 50 Å to 4000 Å are 6 O II and 14 Mg II ground-state transitions. Because PROMETHEUS does not support non-Maxwellian velocity distributions, the absorption lines becomes Voigt, with Maxwellian velocity distribution at $0\,km\,s^{-1}$. For that reason, lines in the spectrum are neither velocity- nor thermal-broadened and are narrow. Without the artificial line-width increase, as explained Sect. 2.2.6, the lines would have their intrinsic FWHM. Nonetheless, the lines have different depths due to different oscillator strengths f. The column-wise optical depth at wavelength of the strongest absorption is shown in Fig. 2.9. We can clearly see the same structure as shown in the column density plot of the fiducial run (Fig. 2.7). A synthetic spectrum of the fiducial run was also produced with Plasmetheus, shown in Fig. 2.10. The same stellar and planetary parameters were used for this simulation. Due to long computation times, only the absorption of the deepest line (Mg II at 2800 Å) was simulated. The absorption depth of this spectrum

[5]Due to stellar variability, the density of the stellar wind is subject to change. For a period of high stellar activity, similar values for the proton density may even be measured at Earth's orbit.

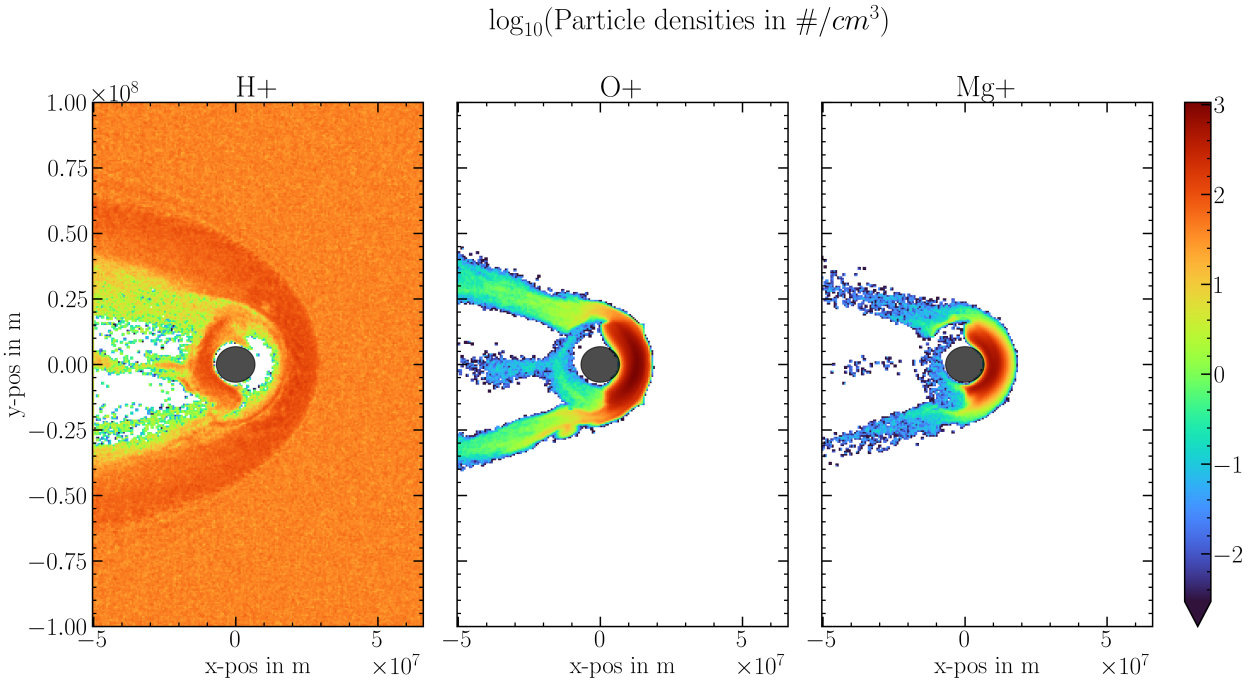

Figure 2.6: Top-down view of particle densities of the centre slice in the fiducial AMITIS run. In this simulation, the protons move at super-magnetosonic speed, creating a bow shock as they collide with the planetary ionosphere. There, ionisation of atmospheric particles lead to a high density region of O II and Mg II, whereas protons cannot enter deeper into the front region of the bow shock. Contained within the extent of the bow are the tails of the planetary ions, which extend several planetary radii behind the planet. In the fiducial run, due to some unknown effect, the source region of the O II particles is too large, and slightly visible as sharp edges in the middle plot, just in front of the planet. The later simulations fixed this issue.

is smaller by factor of seven compared to the one calculated by Prometheus (Fig. 2.8). This is due to the inclusion of particle radial velocity in the spectrum: In Prometheus, all particle Doppler broadening is zero, and all lines are located at exactly the same position. As a result, the spectrum is narrow, and very deep. While the integrated line strength of both spectra remains the same, in Plasmetheus the particles cause a shift in the central line position due to their relative motion to the observer. The distributions of particle velocities thus emerge in the morphology of the lines. Although the intrinsic shape of absorption lines is symmetric, both lines here feature a wider blueshifted tail (towards shorter wavelengths), indicating that a larger fraction of particles are moving towards the observer. However, particles also move away from the observer, likely those close to the planetary surface and on the day-side of the planet, and cause a broadening into the redshifted part of the wings. A shift of the peak of the line away from the line centre indicates a non-zero mode velocity of the absorbing species. For the fiducial run, the peak positions are close to or at the line centre. This is in accordance with the velocity distributions of the ions shown in Fig. 2.4, which are centered around zero. We made several conclusions from the fiducial run for future simulations. Mainly, the narrow width of the lines highlights the importance of taking into consideration the particle velocities. Theoretically, situations in which particles do not accelerate to velocities of $\mathrm{km\,s^{-1}}$ can still yield spectra with absorption peaks with substantial width, due to the saturation in the absorption wings. This effect is further described in Draine (2011, Ch. 9). However, the density of plasma particles in the exosphere is too low to attain this effect. Moreover, the velocity distribution on voxel scales cannot be approximated to be

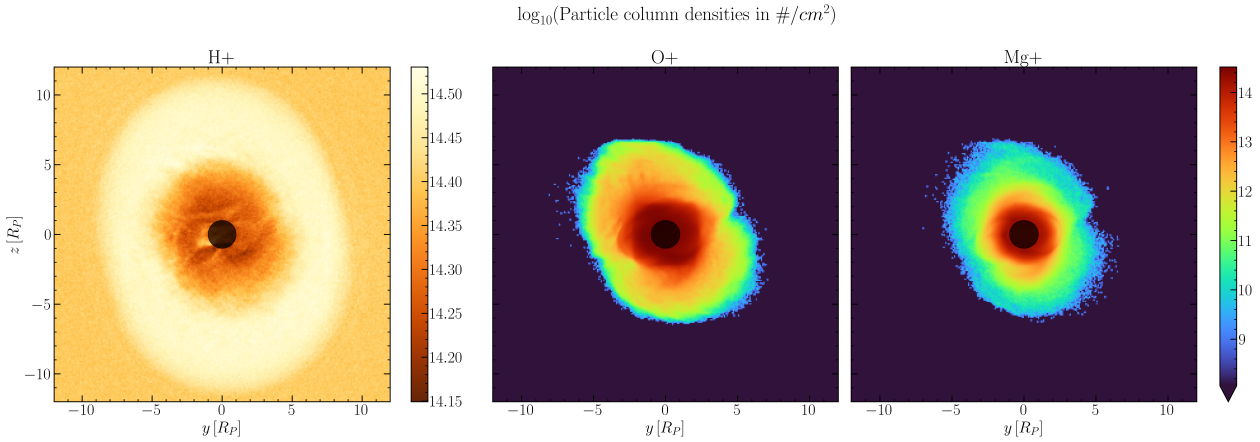

Figure 2.7: Column densities for the fiducial run. Protons feature a tilted ring-like morphology

Gaussian. We compare the absorption depth to observational values in García Muñoz et al. (2021), at 6.7 %. Even with the quadrupled depth presumably reached by adjusting the planetary size to that of π Men c, the result is still one order of magnitude smaller than expected. Differences in the oscillator strength of different species may slightly affect the depth, but are not enough for a change of this scale. Consequently, the size of the exosphere needs to increase to match the observations. Its size depends on the profile of the atmosphere, as well as the stellar wind density. For a planet similar to π Men c, at an orbital distance of 0.06 au, stellar wind density of a G-type star may be higher by orders of magnitude than in the fiducial run.

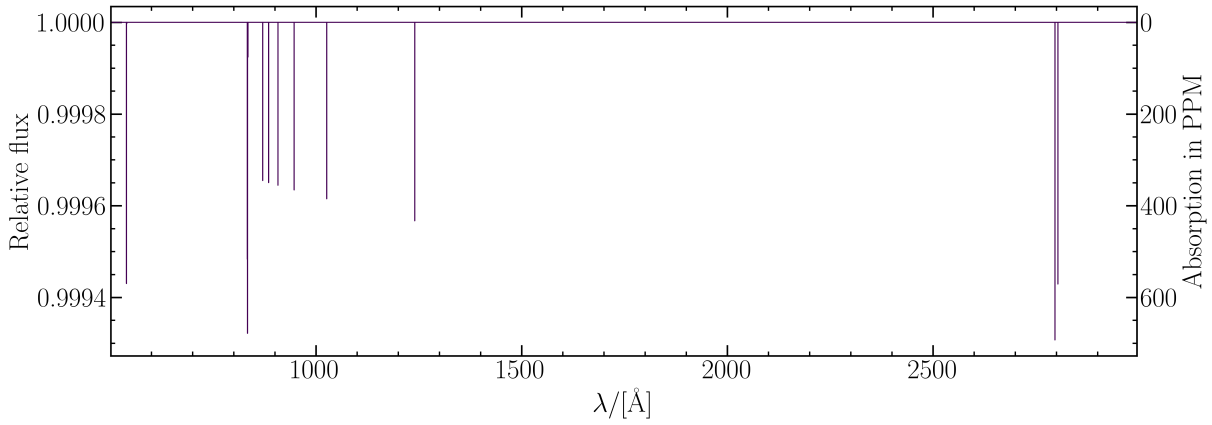

Figure 2.8: Synthetic spectrum of an Earth-like planet (in size, mass and magnetic field) produced by Prometheus. Three of the six O II lines are in the rightmost absorption line, too close to be resolved here. The other three O II lines are at and around the deep line at ≈830 Å. The rest of the spectrum are Mg II absorption, with the deepest line doublet at ≈ 2800 Å. Fig. 2.9 shows the column-wise optical depth at this wavelength. In this spectrum, the position of the lines are correct, but due to the lack of broadening effect, the depth, as well as the morphology of the lines may be incorrect. Nonetheless, it indicates that even an Earth-like planet's exosphere may be detectable, with sufficient SNR.

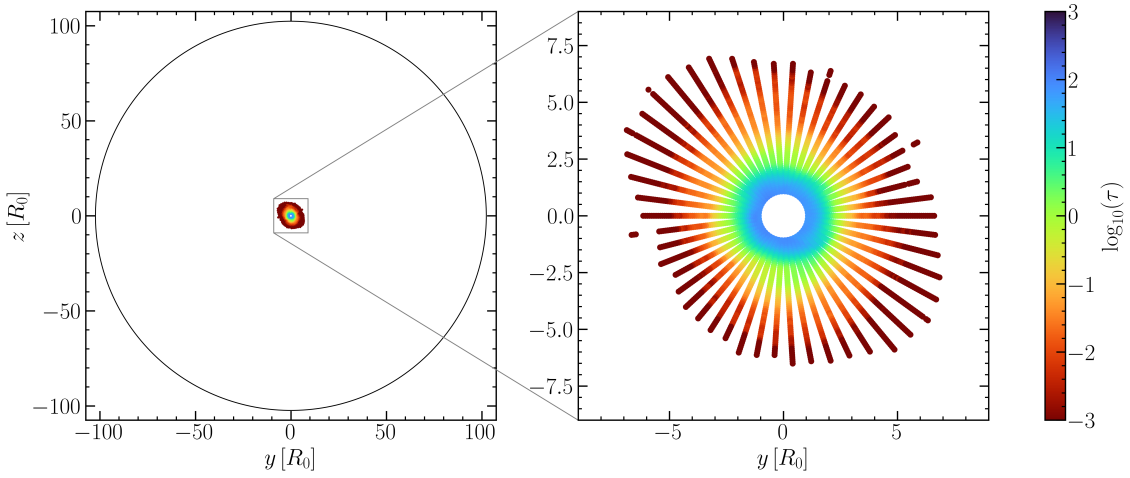

Figure 2.9: The column-wise optical depth of the deepest absorption line in the range 500 Å to 3000 Å, at 2796 Å. In the left picture, we show the correct scale between stellar size, planet size and extent of ionised particles. The right side shows a zoomed-in view of the column actually contributing to the reduction in flux. An area with roughly 3 R_P is optically thick, but the rest of the cloud is optically thin. Prometheus uses a cylindrical instead of a Cartesian grid, hence the structure.

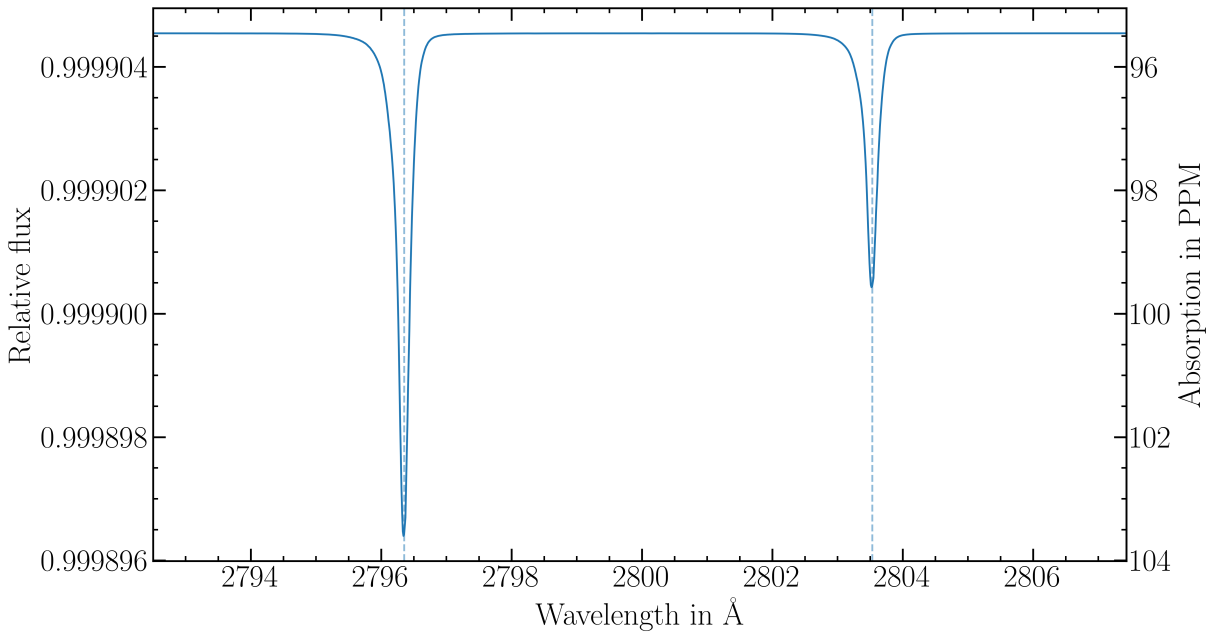

Figure 2.10: Plasmetheus spectrum simulation of the absorption by the Mg II doublet at 2800 Å from the fiducial AMITIS model. The intrinsic line centres are marked with dashed lines. Both lines are broadened to a FWHM of ≈ 0.25 Å. Lines are more shallow than the ones produced in Prometheus, because they are broadened more due to the particle velocity distributions.

Chapter 3

Results and Discussion

We present our main simulation of the planet π Men c, with different stellar and planetary simulation parameters for AMITIS. We start by presenting results for an unmagnetised planet in Sect. 3.1.1, and continue to compare these results with two different magnetised models in Sect. 3.1.2, and discuss the effect of magnetic fields on exosphere morphology and simulated transmission spectra. We then investigate the impact of a different direction in stellar magnetic field in Sect. 3.1.3. Plots for all simulations can be found in the appendix.

3.1 π Men c

Simulations were subsequently run for π Men c. Of the three lines in the triplet covered by García Muñoz et al., only the lowest line is a ground-state transition. Therefore, this is the only line we model as of now. It has similar oscillator strength and Einstein coefficient to the other two lines. While it was not detected due to ISM absorption, we assume the flux change in these two lines to be similar. The stellar size is $1.1\,R_\odot$, and planetary size is $2.04\,R_\oplus$. From previous results (García Muñoz et al., 2021, 2020), we conclude that the atmosphere is poor in hydrogen, and richer in heavier carbon and oxygen. Similar to Venus, the existence of CO_2 as a constituent of the atmosphere follows. We treat π Men c as a super-Venus, scaling the observed profile of carbon and oxygen. Simulation parameters in AMITIS were varied with different planetary magnetic field strengths and stellar magnetic field orientations. We then compare the observational data from García Muñoz et al. (2021), especially the depth and shape of the previously discussed C II absorption line at 1334 Å, to the spectra produced by Plasmetheus. This allows investigation on the effect of a potential planetary magnetic field on the absorption spectrum. Additionally, we can estimate the influence of the Parker spirals on the synthetic spectrum by comparison with a non-angled stellar magnetic field (see Sect. 2.3). In all plasma simulations the stellar wind velocity has a component in negative y-direction, which imitates the planet's velocity around the star and the resulting angle of attack of the protons. Because ions are picked up and entrained in the solar wind, the angle of attack may therefore affect the absorption by other species. On top of these adjustments, these runs also feature a larger number of tracer particles than the fiducial run, to more precisely model the exosphere. The box size was also increased to contain most of the exospheric tails.

3.1.1 Unmagnetized planet

3.1.1.1 AMITIS results

A top-down view of an AMITIS model of unmagnetized π Men c can be see in Fig. 3.1 and Fig. 3.2. In this case, the protons stream with a radial velocity of $550\,km\,s^{-1}$, and a component in negative y-direction of $104\,km\,s^{-1}$. The stellar magnetic field points in positive y-direction (parallel to the motion of the planet),

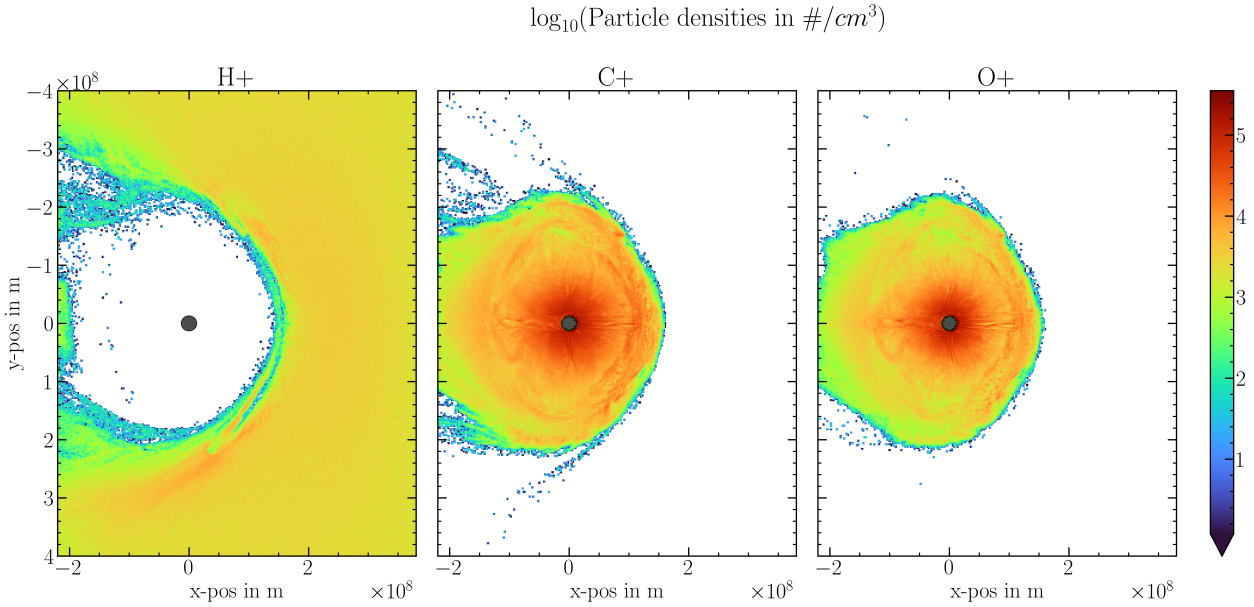

Figure 3.1: Unmagnetised: Side-on single slice view of particle densities in AMITIS plasma model of an unmagnetised π Men c. Horizontal and vertical axes show x- and y-direction of the simulation, respectively. In comparison to the fiducial run, no bow shock is formed. Particle densities peak at 100 000 cm^{-3}.

with a strength of 1500 mT. Contrary to the solar system, where a planet at distances similar to π Men c would experience a magnetic field almost entirely in radial direction, the fast rotating star π Men (Wenger et al., 2000) leads to more tightly wound magnetic field lines. Hence they are almost parallel to the orbit at the distance of π Men c. Immediately apparent is the large extent of the exosphere, with peak densities higher by two orders of magnitude compared to the fiducial run. As the stellar wind is now in the sub-sonic sub-magnetosonic regime (Chiuderi & Velli, 2015), we no longer see the formation of a bow shock. Instead, particle densities of the heavier ions gradually increase towards the planet. Outwards, the density decreases from 100 000 cm^{-3} to 10 000 cm^{-3}. For the planetary ions, horizontal and vertical structures form outwards from the planet. At edge of the ionosphere, we see a soft boundary, where particle densities start to decrease to values between 1000 cm^{-3} to 100 cm^{-3}. Despite not featuring a bowshock, an edge in particle densities can be seen for both C II and O II. Protons slightly increase in density as they hit the ionosphere of the planet. A large region around the backside of the planet is fully devoid of protons, even without a planetary magnetic field shielding from the stellar wind. Formation of two distinct ion wings cannot be clearly seen anymore. We can clearly see entrainment of carbon ions in the stellar wind, from within the high density regions in front of the planet. This effect is also present for ionised oxygen, but less pronounced. The overall shape of the ionosphere is more extended and round than in the fiducial run. The complementary side-on view of this model is shown in Fig. 3.2. Due to the interaction between the magnetic field and the escaping planetary ions, an overdensity develops above the planet, best visible for C II. A detail not visible in Fig. 3.1 is that the area void of protons behind the planet is asymmetric, curving downwards. Overall, the higher particle densities will reflect in the column optical depth, and cause higher absorption of stellar radiation. In addition, the larger extent of the cloud will also cause higher absorption, for appropriate optical depths. Further out in the tails, we likely find high velocity ions, which will cause absorption far out in the blueshifted wings of the absorption line. Depending on the stellar spectrum, this region might be hard to probe, due to low stellar continuum UV flux (Sect. 2.2.7).

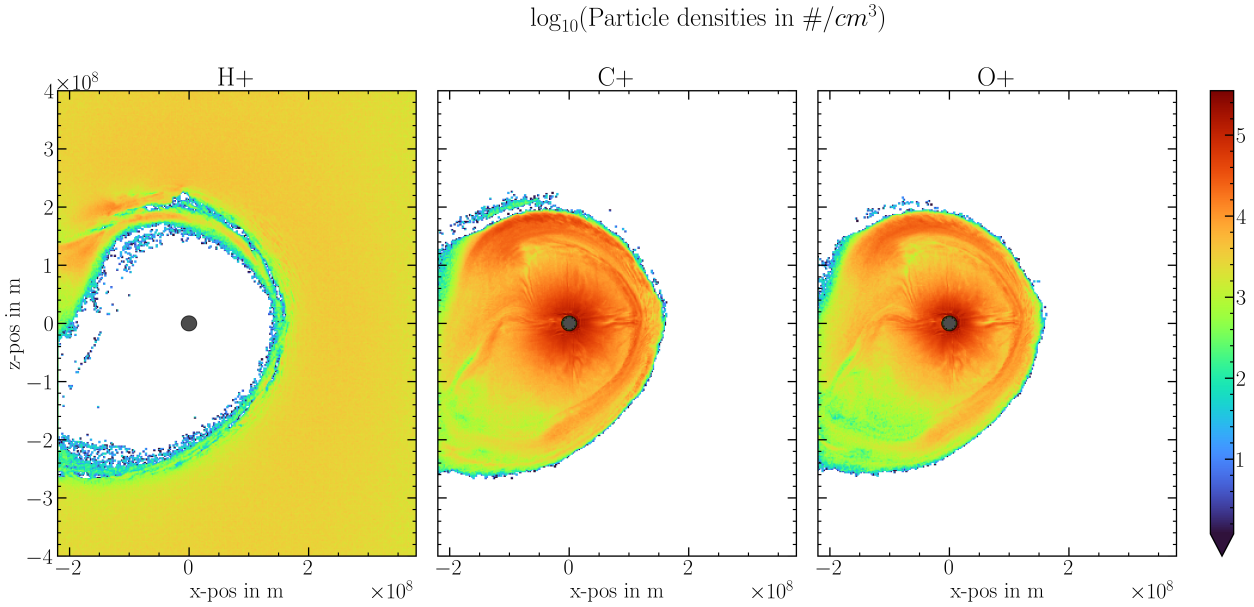

Figure 3.2: Unmagnetised: Single slice view of particle densities in AMITIS plasma model of an unmagnetised π Men c. Horizontal and vertical axes show x- and z-direction of the simulation, respectively. The asymmetry in z-direction is formed due to Lorentz forces on the ions.

3.1.1.2 Plasmetheus spectra

Using this model, we use Plasmetheus to simulate the absorption by C II at 1334 Å, shown in Fig. 3.3. Similar to results from the fiducial run, we observe an asymmetric absorption peak. Absorption depth is higher than before, up to 20 000 ppm (=2%), which is on the order of magnitude of the García Muñoz et al. observations. In contrast to the fiducial run, the centre of the line is offset by 0.5 Å, which corresponds to a mode velocity shift of roughly 100 km s^{-1}. Both offset and asymmetry indicate that a large fraction of particles are moving towards the observer. A slight edge at the location of the intrinsic line centre indicates the existence of a population of particles with 0 km s^{-1}. Due to noise, this detail is unlikely to be seen in observations.

3.1.2 Magnetised planet

3.1.2.1 AMITIS results

The next two simulations in this work aim to investigate the effects of planetary magnetic fields. Together with the non-magnetised planet, they form a set of three plasma simulations, with no intrinsic magnetic field, a low-strength magnetic field and a medium strength magnetic field. The two magnetised planets have dipoles as large as Earth, and therefore the magnetic field at the surfaces are ≈ 1000 nT for the weakly magnetised planet and ≈ 3750 nT for the medium magnetised planet. For comparison, Earth's surface magnetic field has a strength of 31 000 nT at its dipole equator (De Pater & Lissauer, 2015). These numbers are different due to different planetary sizes. The orientation of the stellar magnetic field is solely in y-direction, and the dipole of the magnetised planet points in negative z-direction. Earth's magnetic dipole has a tilt of 10° relative to its rotation axis (De Pater & Lissauer, 2015). We show the particle densities of the medium magnetised planet in Fig. 3.4.

Again, no bow shock is visible, as the parameters of the stellar wind did not change. The shape of the planetary ionosphere is more spherical, and its radial extent is reduced compared to the unmagnetised planet. Protons also extend less deep into the ionosphere, as seen by lower proton density on the edge of it. The

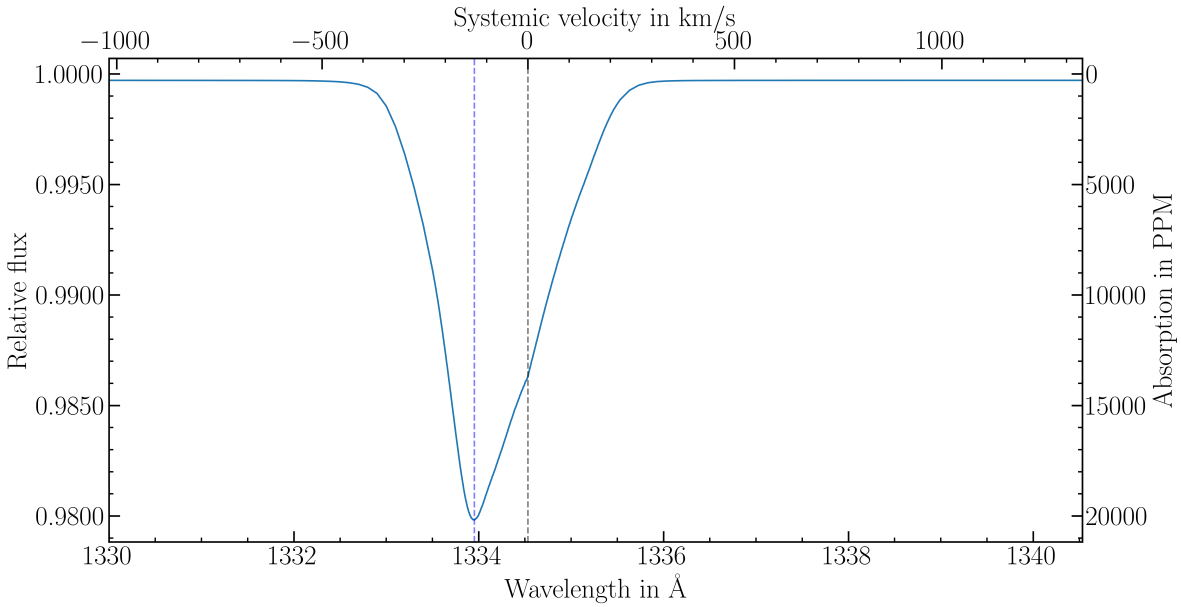

Figure 3.3: Absorption at 1334 Å from C II around pi Men c. For these runs, the maximum absorption depth is at 20 000 ppm, or 2%. This is comparable to the observation in García Muñoz et al. (2021). An offset of the peak indicate a mode velocity of roughly $-100\,\mathrm{km\,s^{-1}}$ for the C II particles. At the intrinsic line centre, a slight bump is visible, likely due to a population of particles streaming off the planetary surface with $0\,\mathrm{km\,s^{-1}}$ radial velocity.

morphology of planetary ion wings is more pronounced than in the unmagnetised simulation, but still weak compared to the fiducial run. A side on view of this plasma model is shown in Fig. 3.5. Compared to the similar plot for the unmagnetised planet, a clear difference is that no inner edge of particle densities is visible for the planetary ions: Both in Fig. 3.2 and Fig. 3.1, a density edge is visible at roughly $1\,R_P$ for carbon and oxygen. Furthermore, spherical morphologies within the ionosphere suggest circular movement of planetary ions. For atmospheric escape, this ties well into the observations of recycled oxygen in Earth ionosphere (Seki et al., 2001).

The change in exospheric extent is well visible in the column particle densities, shown in Fig. 3.6. It shows the column number density of C II-ions for all three simulations. The size of the exosphere is smaller for the magnetised planets, since the magnetosphere of those planets shields it from the stellar wind. For all three planets, a roof-like structure is visible. It is created by the Lorentz forces (Eq. (2.1)): the particles move towards the observer, and the magnetic field lines are parallel to the orbit of the planet. As a result, the Lorentz force acts upwards on the ions, creating the "roof". The "roof" itself also shows asymmetries along the y-axis, likely due to the angle of attack of stellar wind protons. Planetary particles ionise close to the planet and escape the lower part of the atmosphere. From there, they interact with the ionosphere, and move upwards, where they are entrained in the stellar winds. This gives them a component in negative y-direction, which leads to asymmetries in the "roof". The difference in size is very apparent when comparing the unmagnetised to the magnetised planets, but a distinction within the magnetised models is hard to make. Likely, the difference in magnetic field strength between the two models is not sufficient to cause a clear size difference in the exosphere, since magnetic shielding is similar in both cases.

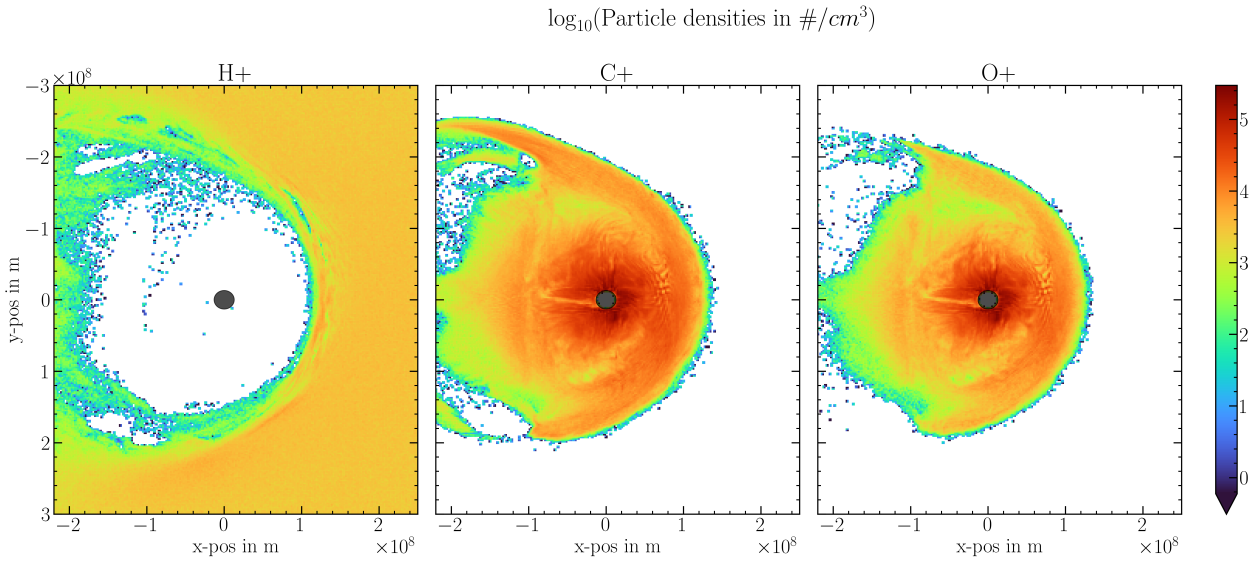

Figure 3.4: Medium dipole: Particle densities of AMITIS simulation of π Men c. Compared to the unmagnetised planet, shape of the ionosphere is more spherical. The protons densities on the edge of the ionosphere are lower. Wings of the planetary ions are more pronounced than before.

3.1.2.2 Plasmetheus spectra

We show the three spectra of the O II line in Fig. 3.7, where we normalised the maximum absorption to that of the medium dipole planet. Without this correction, the unmagnetised planet has the largest absorption depth, at 2 %, while both the weak and medium dipole only reach up to 1.4 %. Overall, the line morphology is similar for all three planets. The position of absorption line peak is dependant on the planetary magnetic field. While the difference is small, we can nonetheless clearly see that the higher the intrinsic magnetic field strength, the lower the blueshift of the exospheric spectrum. This agrees with the previous suggestion that the planetary magnetic field shields the planet from the stellar wind. In detail, particles are accelerated less quickly by the protons. While absorption line shape is a bad indicator for magnetic field strength, with known stellar wind parameters and stellar magnetic field, the offset of absorption lines of ions may be used to infer the planetary magnetic field strength. For even stronger magnetic fields for super-Earths like π Men c, judging purely by size, this effect may even be stronger than suggested by our simulations. On the other hand, this assessment is limited, since lines will not be moved further than close to $0\,\mathrm{km\,s^{-1}}$, even for extremely strong planetary magnetic fields and strong stellar wind shielding.

3.1.2.3 Optical depth

To investigate the absorption within the exosphere, we compare the column-wise optical depths at the maximum absorbing wavelength for two simulations. Fig. 3.8 shows the optical depths for the unmagnetised and medium dipole π Men c, respectively. Areas with an optical depth $\tau > 1$ are considered optically thick, and coloured in, while anything with $\tau < 1$ is mapped to a grey scale. Despite the high particle column densities shown in Fig. 3.6, only two regions contain optically thick columns for both simulations. Note that the maximum absorbing wavelengths is different for these two simulations, and thus the corresponding particle velocities are also different. For the unmagnetised planet, the shift corresponds to a velocity of roughly $-130\,\mathrm{km\,s^{-1}}$, and for the medium dipole $100\,\mathrm{km\,s^{-1}}$. Hence, these two plots highlight slightly different populations of particles. It is interesting that particles moving at high velocities ($\approx 100\,\mathrm{km\,s^{-1}}$) are also found close to the planetary surface. Because these regions are still inside the ionosphere/magnetosphere of the

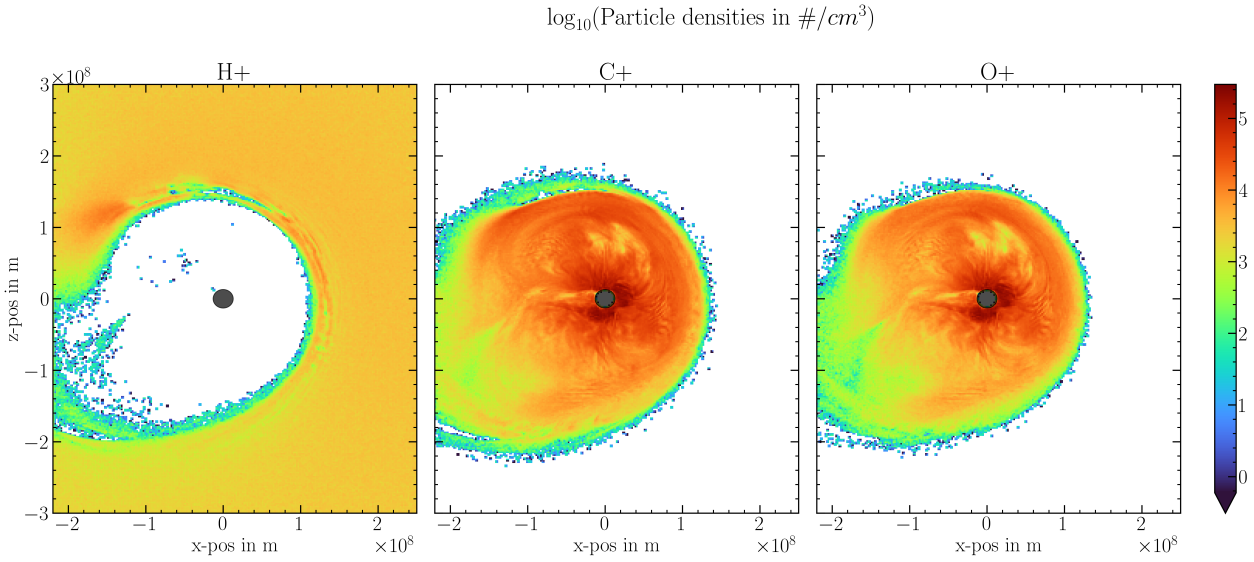

Figure 3.5: Medium dipole: Side-on view of particle densities for a planet with a medium dipole. The ionosphere resembles an "egg-like" or a "teardrop" shape. Behind the planet, this shows as a ion tail that is displaced downwards. In the cavity, the density of protons is higher than the mean density within the interplanetary medium. For C II and O II, the area above the planet shows higher particle densities. Swirls in the density structure of these species suggest some sort of circular movement.

planet, ions may not be accelerated by stellar wind, but through other means instead. Theoretically, they could also be entrained in the stellar wind, but through interactions with magnetic field return to columns closer to the planet[1]. For both simulations, the optically thick region above the planet corresponds to the high density regions ("roof") described before. These regions therefore are important when evaluating the absorption of the exosphere: They are regions of high particle densities, and particles must have similar velocities in order to absorb at the same wavelengths. As a result, the impact of magnetic field interactions must not be ignored. Once again, the angle of attack of stellar wind protons is likely the cause of the displacement of high-density (and high opacity) regions. We would like to note that despite this choice of colormaps, the grey shaded region still contributes to the absorption. Especially for values close to one, their contribution is presumably very large due to their large area. This plot rather highlights regions in which higher particle density contributes less significantly to an increase in absorption depth. Since this area is quite small for both of these models, to first order approximation, increasing the particle density also could increase the absorption depth by the same relative amount.

3.1.3 Parker spiral effects

In another AMITIS simulation, we keep an unmagnetised planet, and only change the angle of the stellar magnetic field to imitate Parker spirals. We compare the two results in Fig. 3.9. Note that the simulation of the non-angled magnetic field is not the same as before: AMITIS box sizes were not large enough to contain the whole ionospheric tail for these two models. Due to time constrains, we were unable to rerun the models with larger box lengths. These results have to be interpreted carefully. The bump at the line centre is smoothened, and maximum line depth is increased. The shape of the two absorption lines is similar, with an offset to roughly $90\,\mathrm{km\,s^{-1}}$. Wings of the perpendicular magnetic field model are slightly wider than that of the Parker spiral model, but this effect is not very pronounced and is not expected to be visible in

[1] relative to the observer

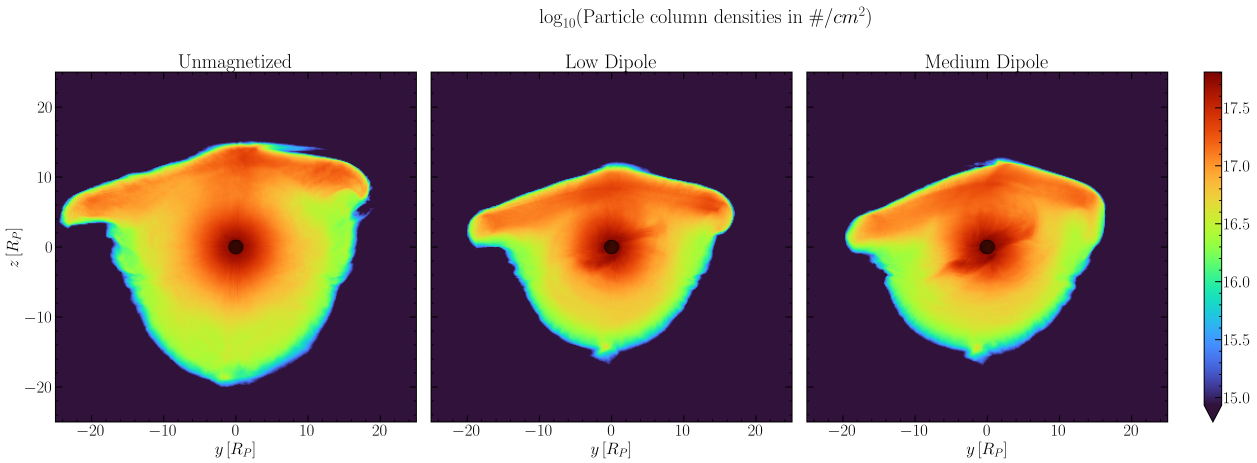

Figure 3.6: Column density of C II for an unmagnetised, low dipole and medium dipole model. The difference in size of the exosphere for an unmagnetised to a magnetised planet is very apparent. A "roof", i.e. an asymmetry in exosphere morphology is visible for all three planets, as a result from Lorentz forces. Within the roof, particle densities are slightly higher.

observations. The decrease of the bump at the intrinsic line centre at $0\,\mathrm{km\,s^{-1}}$ implies less visible particles at rest relative to the observer. They may then be covered by the planetary shadow. It appears that the Parker spiral influences the morphology of the exosphere, especially close to the planet. Since the maximum absorption wavelength is similar, the effects of Parker spirals on the position of peak absorption are less significant than that of a planetary magnetic field. If these differences were measurable, it might give insight into the stellar wind velocity at the orbital distance of the planet, since the angle of the Parker spiral is dependant on the stellar wind velocity. An increase in absorption depth by 25 % is nonetheless remarkable, and might help in reproduction of observed transit depth of π Men c. Because of the issue with the box side length in these two models, this result has to be taken with a grain of salt.

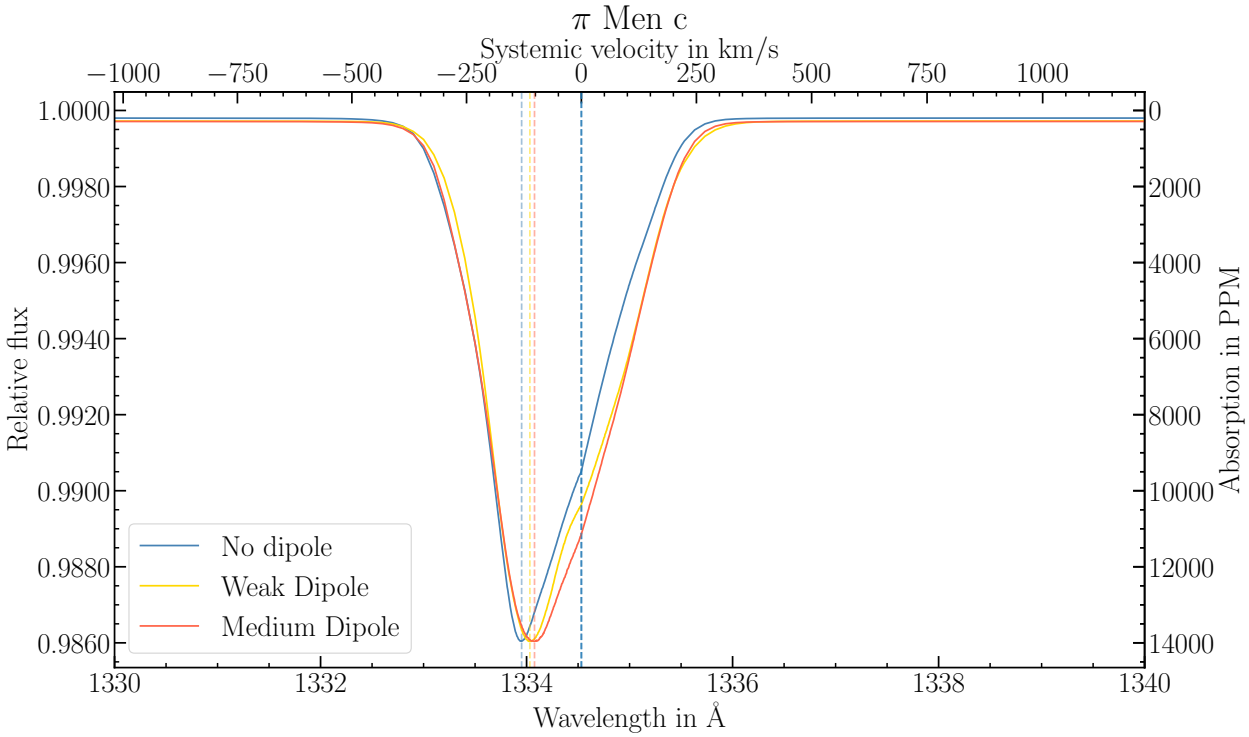

Figure 3.7: Synthetic transmission spectrum of the C II line at 1334 Å for three simulations only different in magnetic dipole strength. The signals were normalised to the medium dipole model. It can be seen that the blueshift of the absorption peak is smaller for higher magnetic field strength. Furthermore, the edge at $0\,\mathrm{km\,s^{-1}}$ is less pronounced for the medium dipole model, but more pronounced for the weak dipole model.

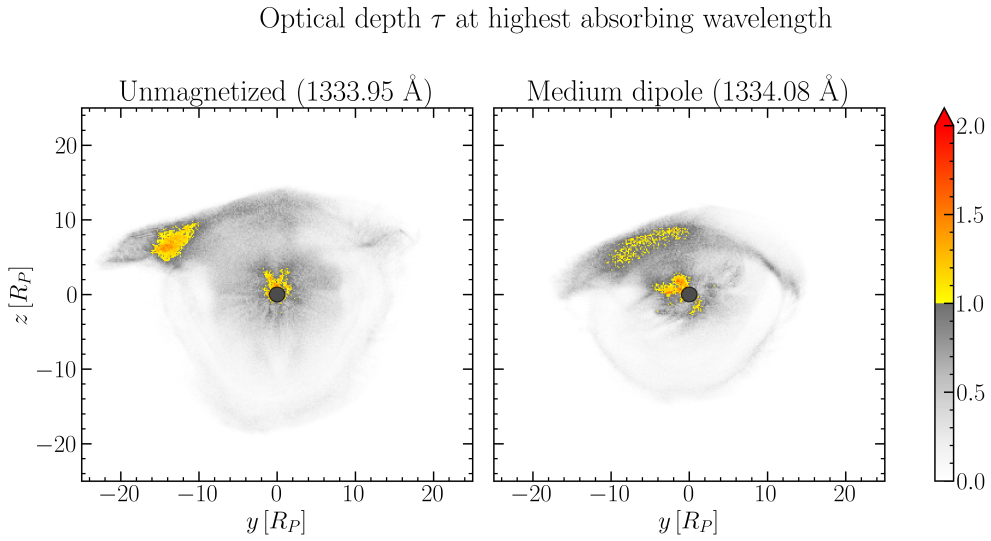

Figure 3.8: Optical depth of planets with no dipole and medium dipole, at their respective highest absorbing wavelengths. Regions that are optically thin are coloured in a grey scale, and region optically thick with a coloured one. For both simulations, two main optically thick regions are present: Close to the planet, up to $\approx 4R_P$ in radius, and further out on the edge of the ionosphere. Different regions are highlighted compared to 1a and 1c. Regions of high optical depth at the respective wavelengths are high in particle density, and particles within these regions move at similar velocities.

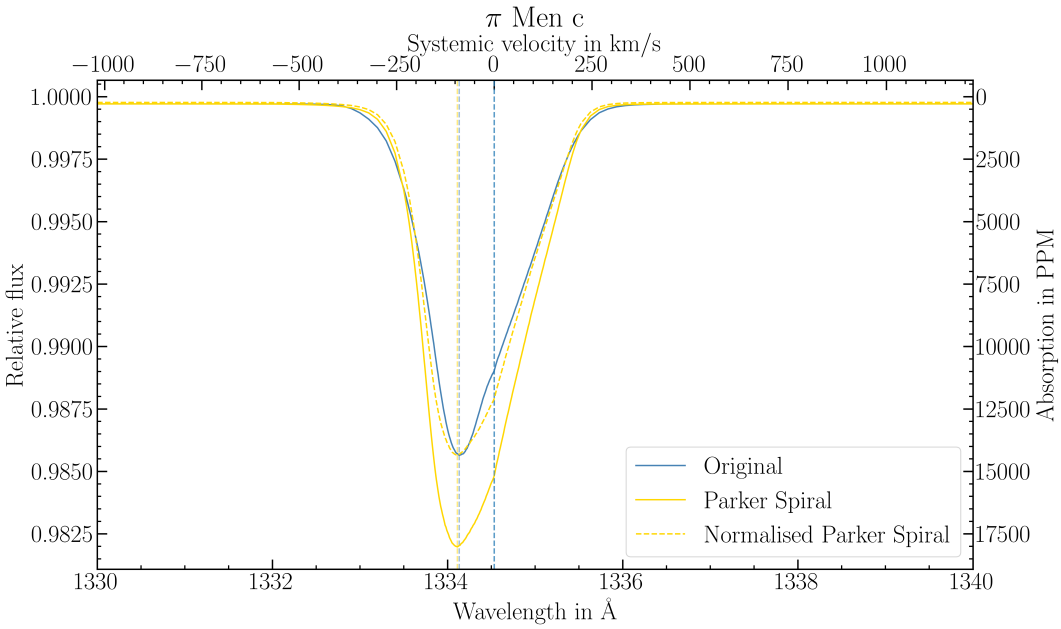

Figure 3.9: Comparison of the C II absorption line for a perpendicular and an angled (Parker spiral) stellar magnetic field. These two unmagnetised models are different from the previously presented simulation: Here, the AMITIS box length was too small to contain the whole ionospheric tail. Due to time constraints, we were unable to rerun this set of simulations. This may compromise the validity of this result. The yellow dashed line is the Parker spiral simulation normalised to the original. It seems that an angled magnetic field changes absorption line morphology around $0\,\mathrm{km\,s^{-1}}$. The line depth is increased by 25 %.

Chapter 4

Conclusions

We used plasma models of the super-Earth π Men c to calculate synthetic absorption spectra of the 1334 Å C II line in its exosphere. As a proof of concept, we show that the results are similar to that observed by García Muñoz et al. (2021). In this final section, we discuss details of the theory and the methodology that influence the results. Doing this, we provide new ideas for future research on exoplasma simulations.

4.1 Comparison to observations

One of the goals of this work was to reproduce the observations made by García Muñoz et al. (2021). The main limitation of this project is the current inability to model non-ground-state transitions. This is especially important since two of the three lines observed by García Muñoz et al. are non-ground-state transitions. As detection of absorption in the third line was hindered by absorption through the ISM, this limits our reproducability in observations. We therefore made the assumption that the absorption strength from the ground state transition is similar to that of the upper two lines, if it was visible. This might not be true, depending on the plasma physics and the atomic energy difference between the levels: If the ground-state transition has a lower multiplicity, it may be less occupied compared the other two transitions. As a result, the absorption in this line would be reduced. However, if they are similar, then we were able to reproduce absorption in the line on a similar scale (2 %). This number could be increased by various methods.

First and foremost, changing the atmospheric profile and thereby the ion source rates could increase the column particle density and therefore the optical depth. In our current simulations, our ion densities are below the upper limit suggested by García Muñoz et al.. Increasing the source rate will also affect the planetary ionosphere and thus the morphology of the cloud. It may well be that at some point, increasing the source rate leads to a decrease in absorption depth, since the induced magnetic field effects of the ions reduce the extend of the exosphere. Higher particle densities close to the planet no longer increase absorption depth, since the columns are already optically thick. Lower particle densities further out decrease the absorption depth, since these regions are optically thin. Further runs with higher source rates are necessary to investigate here. The change in optical depth due to an increase in particle number will also depend on whether the columns affected by the increase are already optically thick or not. If the absorption is mainly caused by a small area with optically thick columns, further increasing the particle density in those columns will not increase absorption significantly. To increase absorption there, it has to be spread over a larger area. This could be accomplished by increasing the scale height of the atmosphere, or decreasing the planetary magnetic field. In the current models however, it is clear that a large part of the exosphere is still optically thin, so the necessary increase in absorption could be accomplished by increasing the ion source rates.

The simple model used by García Muñoz et al. assumes an exosphere with a radius of 15 R_P. According to our results, this is a decent approximation for both a non-magnetised and a medium dipole planet. But for a planet with a higher magnetic dipole, the exosphere might be considerably smaller. We do not consider

further ionisation by stellar radiation or stellar wind. In the case of photoionisation, with a lifetime of C II ions of $\approx 20\,\mathrm{h}$, at velocities around $-100\,\mathrm{km\,s^{-1}}$, the ions would escape the exosphere and the range of observation before ionising. If we assume charge exchange to reduce the number of C II ions, the reduction in flux would be apparent for the far blueshifted part of the absorption line. These effects are therefore small, especially when considering the low continuum flux in the UV.

In contrast to García Muñoz et al. we do not assume a Voigt line profile. Our results still agree with the dominance of the bulk Doppler shift through acceleration mechanism in the exosphere over thermal line broadening. Changing the intrinsic width of the line also helped to create a more realistic spectrum. However, in our simulations, it is still important to consider the distribution of particle velocities, as mentioned before. We find that several parameters impact the observable absorption peak significantly. This implies that values for the ionisation timescale found by García Muñoz et al. may be incorrect.

Furthermore, the mode velocity of ions is greatly affected by the presence of a planetary magnetic field. To constrain the magnetic field strength of π Men c, several steps are necessary: Firstly, multiple transit observations of the C II line would cover different periods of stellar winds intensity of the host star. Second, further modelling with different atmosphere profiles and magnetic field strengths will yield different shifts in the absorption peak. If we assume the particle loss rate to be constant throughout our observations, then fitting different models to these observations can help us constrain the dipole of the planet.

4.2 AMITIS models

We mentioned that the plasma models produced by AMITIS are run until the changes within the model are small for hundreds of seconds. However, with the low number of models currently available it is still unclear whether different types of semi-stable states can be reached. If possible, those might result in different exosphere morphologies and absorption spectra. Also, changes in the stellar wind strength, as known here on Earth, are not included in the simulations. Over the course of transit observations, the effect of small scale variability (on the scale of minutes) in the stellar wind will be averaged over. In order to account for the effects of variability on longer timescale, simulations with slight variation in stellar wind parameters (temperature, velocity, direction) are necessary. Furthermore, we see in our visualisation that the exosphere extends beyond the modelled region, i.e. the simulation box is too small. Increasing the length of the box also lead to an increase in absorption depth of 30 %. This implies that these regions are still important. When considering further ionisation of particles, this effect would be reduced. Contribution of the regions very far away from the planet are assumed to be small due to low particle densities. Knowing that at these location particles have likely accelerated to velocities on the order of several hundred $\mathrm{km\,s^{-1}}$, these regions contribute to the far blueshifted wings of the absorption lines. This may not be significant for mid-transit observation, but could affect egress observations.

4.3 Ions and transitions

Future models would greatly benefit from the inclusion of non ground-state transitions. Further research and expertise is needed to explore this possibility. The multiplicities of the different levels depend on the temperature of the medium. However, since we are dealing with non-collisional regimes, this complicates the theory. For the two upper C II lines, the lower energy state is almost at 0. It is important to examine whether the energy difference between low energy state and ground state could be provided by stellar radiation. This may then allow us to treat both levels as ground states. Future simulations could easily implement this idea. The simulations would also benefit by further modelling of ionisation of species in the stellar wind, as done by García Muñoz et al.. By assuming an exponential ionisation depending on position along the line-of-sight, species like C III could then also be included in the simulations. However, we expect the absorption of in these lines to be less due to the non-uniform acceleration processes.

4.4 Simulation parameter space

In the scope of this work, only a small sector of the available parameter space was explored. In further research, the main parameters to explore are stellar wind density and speed, larger planetary magnetic fields and changes in the ion source rate and scale height. Different combination of these parameters may reveal further interesting properties of exospheres. Particle densities could be increased until the soft upper boundary set by García Muñoz et al. (2021) is reached in the vicinity of the planet. A change in scale height is not expected to significantly alter the absorption depth significantly, since the largest part of the exosphere is optically thin. This might change for higher particle densities than probed here. Also, changing the scale height could matter for simulations in which the exosphere is smaller. Here, the same number of particles would be confined to a smaller area, due to e.g. a higher stellar wind proton density or a stronger planetary magnetic field. In order to test the validity of the results on the effects of Parker spirals, these models would have to be rerun with larger box lengths. Once again, the angle of Parker spirals also depends on the local velocity of the protons. Additionally, comparing Parker spiral models on different magnetised planets would be important to consider, because the decrease in absorption due to higher magnetic shielding could be buffered by the effects of the spirals.

4.5 Plasmetheus adaptations

The next step of radiative transfer calculation would be to include the whole transit event, i.e. from ingress to egress. This could be done by a simple rotation of the 3D box provided by AMITIS. Changes in radial velocity of the planet could reveal more parts of the extended exosphere. As mentioned before, the narrow stellar lines in the UV could also help to scan the exosphere. As a continuation of this project, a faster code would benefit further research, especially when considering more transitions, a larger wavelength range and more species. This ties well into the computational development.

List of Abbreviations

AMITIS Advanced Modelling Infrastructure in Space Simulations

au Astronomical Unit

FWHM Full Width at Half Maximum

HAT Hungarian-made Automated Telescope

HST Hubble Space Telescope

IAU International Astronomical Union

IR Infrared

ISM Interstellar Medium

JWST James Webb Space Telescope

MS Main Sequence

Prometheus PRObing Mass loss in Exoplanetary Transits with Hydrostatic, Evaporative and User-defined Scenarios

RV Radial Velocity

SNR Signal-to-noise ratio

UV Ultraviolet

VLT Very Large Telescope

WASP Wide Angle Search for Planets

XUV Extreme Ultraviolet

Bibliography

Astudillo-Defru N., et al., 2017, A&A, 602, A88

Batalha N. M., et al., 2011, ApJ, 729, 27

Ben-Jaffel L., et al., 2022, Nature Astronomy, 6, 141

Berta Z. K., et al., 2012, ApJ, 747, 35

Brace L. H., Kliore A. J., 1991, Space Sci. Rev., 55, 81

Brace L. H., Kasprzak W. T., Taylor H. A., Theis R. F., Russell C. T., Barnes A., Mihalov J. D., Hunten D. M., 1987, J. Geophys. Res., 92, 15

California Institute of Technology 2023, NASA Exoplanet Archive, https://exoplanetarchive.ipac.caltech.edu/, [Online; accessed 22-April-2023]

Chapman S., 1931, Proceedings of the Physical Society, 43, 26

Charbonneau D., Brown T. M., Latham D. W., Mayor M., 2000, ApJ, 529, L45

Chiuderi C., Velli M., 2015, Shocks. In: Basics of Plasma Astrophysics. Springer Milan, Milano, pp 181–202, doi:10.1007/978-88-470-5280-2_8

Cosentino R., et al., 2012, in McLean I. S., Ramsay S. K., Takami H., eds, Society of Photo-Optical Instrumentation Engineers (SPIE) Conference Series Vol. 8446, Ground-based and Airborne Instrumentation for Astronomy IV. p. 84461V, doi:10.1117/12.925738

Damasso M., et al., 2020, A&A, 642, A31

De Pater I., Lissauer J. J., 2015, Planetary sciences, updated second edition edn. Cambridge University Press, Cambridge, https://www.cambridge.org/se/academic/subjects/physics/computational-science-and-modelling/planetary-sciences-2nd-edition-1?format=HB&isbn=9781107091610

Dorn R. J., et al., 2014, The Messenger, 156, 7

Draine B. T., 2011, Physics of the interstellar and intergalactic medium. Princeton series in astrophysics, Princeton University Press, Princeton, N.J.

Driscoll P., Bercovici D., 2013, Icarus, 226, 1447

Exoplanet.eu 2022, The Extrasolar Planets Encyclopaedia, http://exoplanet.eu/, [Online; accessed 12-December-2022]

Fatemi S., Poppe A. R., 2018, Geophysical Research Letters, 45, 39

Fatemi S., Poppe A. R., Delory G. T., Farrell W. M., 2017, in Journal of Physics Conference Series. p. 012017, doi:10.1088/1742-6596/837/1/012017

Fatemi S., Poppe A. R., Barabash S., 2020, Journal of Geophysical Research (Space Physics), 125, e27706

Fatemi S., Poppe A. R., Vorburger A., Lindkvist J., Hamrin M., 2022, Journal of Geophysical Research (Space Physics), 127, e29863

Feinstein A. D., et al., 2023, Nature, 614, 670

Gaia Collaboration et al., 2022, arXiv e-prints, p. arXiv:2206.05595

Gandolfi D., et al., 2018, A&A, 619, L10

García Muñoz A., Youngblood A., Fossati L., Gandolfi D., Cabrera J., Rauer H., 2020, ApJ, 888, L21

García Muñoz A., Fossati L., Youngblood A., Nettelmann N., Gandolfi D., Cabrera J., Rauer H., 2021, ApJ, 907, L36

Gebek A., Oza A. V., 2020, MNRAS, 497, 5271

Greene T. P., Bell T. J., Ducrot E., Dyrek A., Lagage P.-O., Fortney J. J., 2023, Nature, p. arXiv:2303.14849

Grießmeier J.-M., 2015, in Lammer H., Khodachenko M., eds, Astrophysics and Space Science Library Vol. 411, Characterizing Stellar and Exoplanetary Environments. p. 213, doi:10.1007/978-3-319-09749-7_11

Henry G. W., Marcy G. W., Butler R. P., Vogt S. S., 2000, ApJ, 529, L41

Hori Y., Ogihara M., 2020, ApJ, 889, 77

Huang C. X., et al., 2018, ApJ, 868, L39

Jones H. R. A., Paul Butler R., Tinney C. G., Marcy G. W., Penny A. J., McCarthy C., Carter B. D., Pourbaix D., 2002, MNRAS, 333, 871

King G. W., Wheatley P. J., Bourrier V., Ehrenreich D., 2019, MNRAS, 484, L49

Kislyakova K. G., Holmström M., Lammer H., Odert P., Khodachenko M. L., 2014, Science, 346, 981

Knutson H. A., et al., 2014, ApJ, 794, 155

Kramida A., Ralchenko Y., Reader J., NIST ASD Team 2022, NIST Atomic Spectra Database (version 5.10), [Online]; accessed Mon Feb 27 2023, doi:10.18434/T4W30F, https://physics.nist.gov/asd

Kulow J. R., France K., Linsky J., Loyd R. O. P., 2014, ApJ, 786, 132

Lavie B., et al., 2017, A&A, 605, L7

Lecavelier des Etangs A., Lissauer J. J., 2022, New Astron. Rev., 94, 101641

Leggett S. K., et al., 2019, ApJ, 882, 117

Lin D. N. C., Bodenheimer P., Richardson D. C., 1996, Nature, 380, 606

Liu M. C., Dupuy T. J., Ireland M. J., 2008, ApJ, 689, 436

Loyd R. O. P., et al., 2023, AJ, 165, 146

Mainzer A., et al., 2011, ApJ, 726, 30

Mayor M., Queloz D., 1995, Nature, 378, 355

McClintock W. E., et al., 2009, Science, 324, 610

Mugnai L. V., et al., 2021, AJ, 161, 284

Niemann H. B., Kasprzak W. T., Hedin A. E., Hunten D. M., Spencer N. W., 1980, J. Geophys. Res., 85, 7817

Owen J. E., Wu Y., 2017, ApJ, 847, 29

Pepe F., et al., 2021, A&A, 645, A96

Perryman M. A. C., 2011, The exoplanet handbook. Cambridge University Press, Cambridge, http://www.loc.gov/catdir/enhancements/fy1114/2011377997-b.html

Prölss G. W., cop. 2004, Physics of the Earth's space environment. Springer, Berlin

Ridden-Harper A. R., et al., 2016, A&A, 593, A129

Ridden-Harper A. R., Snellen I. A. G., Keller C. U., Mollière P., 2019, A&A, 628, A70

Sanchis-Ojeda R., et al., 2015, ApJ, 812, 112

Schneider J., Rauer H., Lasota J. P., Bonazzola S., Chassefiere E., 1998, in Rebolo R., Martin E. L., Zapatero Osorio M. R., eds, Astronomical Society of the Pacific Conference Series Vol. 134, Brown Dwarfs and Extrasolar Planets. p. 241

Seager S., Sasselov D. D., 2000, ApJ, 537, 916

Seki K., Elphic R. C., Hirahara M., Terasawa T., Mukai T., 2001, Science, 291, 1939

Sharp C. M., Burrows A., 2007, ApJS, 168, 140

Showman A. P., Guillot T., 2002, A&A, 385, 166

Tsiaras A., et al., 2016, ApJ, 820, 99

Vidal-Madjar A., Lecavelier des Etangs A., Désert J. M., Ballester G. E., Ferlet R., Hébrard G., Mayor M., 2003, Nature, 422, 143

Vidal-Madjar A., et al., 2004, ApJ, 604, L69

Vidal-Madjar A., et al., 2013, A&A, 560, A54

Wallace L., Barth C. A., Pearce J. B., Kelly K. K., Anderson Donald E. J., Fastie W. G., 1970, J. Geophys. Res., 75, 3769

Wenger M., et al., 2000, A&AS, 143, 9

Wolszczan A., Frail D. A., 1992, Nature, 355, 145

Wordsworth R., Kreidberg L., 2022, ARA&A, 60, 159

de Wit J., et al., 2016, Nature, 537, 69

dos Santos L. A., Bourrier V., Ehrenreich D., Kameda S., 2019, A&A, 622, A46

Appendices

Element	**Ionisation state**	**Wavelength (Å)**	$A_{ul}(\mathrm{s}^{-1})$	f_{ul}
C	2	516.54	4.25e+07	3.40e-03
C	2	518.15	7.33e+07	5.90e-03
C	2	520.20	5.05e+07	4.10e-03
C	2	522.99	6.59e+07	5.40e-03
C	2	526.85	3.73e+07	3.10e-03
C	2	530.27538	4.28e+08	3.61e-02
C	2	533.7507	3.6e+08	3.1e-02
C	2	538.4075	1.4e+07	6.e-04
C	2	541.44490	3.1e+03	2.7e-07
C	2	543.2578	3.95e+08	3.49e-02
C	2	549.31959	6.72e+07	6.08e-03
C	2	549.37844	2.68e+08	1.21e-02
C	2	551.68083	2.4e+07	1.12e-03
C	2	560.23887	6.05e+08	5.69e-02
C	2	576.8745	4.7e+07	2.3e-03
C	**2**	**594.7985**	**1.11e+09**	**1.18e-01**
C	2	635.99456	1.01e+08	6.11e-03
C	**2**	**687.05266**	**2.36e+09**	**3.34e-01**
C	2	858.09180	1.49e+08	1.64e-02
C	**2**	**903.6232**	**6.78e+08**	**1.66e-01**
C	**2**	**903.9615**	**2.70e+09**	**3.31e-01**
C	**2**	**1036.3377**	**7.38e+08**	**1.19e-01**
C	**2**	**1334.5326**	**2.41e+08**	**1.29e-01**
C	2	2324.236	1.40e+00	2.27e-09
C	2	2325.430	5.99e+01	4.86e-08
Mg	2	870.3317	1.04e+06	2.35e-04
Mg	2	870.3463	1.08e+06	1.22e-04
Mg	2	884.6967	1.38e+06	3.24e-04
Mg	2	884.7189	1.44e+06	1.68e-04
Mg	2	907.3752	1.94e+06	4.78e-04
Mg	2	907.4115	2.02e+06	2.49e-04
Mg	2	946.7033	2.69e+06	7.22e-04
Mg	2	946.7694	2.81e+06	3.78e-04
Mg	2	1025.9681	3.43e+06	1.08e-03
Mg	2	1026.1134	3.63e+06	5.72e-04
Mg	2	1239.9253	1.35e+06	6.21e-04
Mg	2	1240.3947	1.52e+06	3.51e-04
Mg	**2**	**2796.352**	**2.60e+08**	**6.08e-01**
Mg	**2**	**2803.531**	**2.57e+08**	**3.03e-01**
O	2	539.0861	9.83e+08	6.42e-02
O	2	539.5473	9.81e+08	4.28e-02
O	2	539.8540	9.81e+08	2.14e-02
O	2	832.7583	8.67e+08	4.51e-02
O	2	833.3303	8.65e+08	9.01e-02
O	**2**	**834.4654**	**8.61e+08**	**1.35e-01**

Table 1: Line list of ground-state transitions ($E_l = 0$) for C II, Mg II and O II. Transitions with $f_{ul} > 1e-1$ are set in bold.

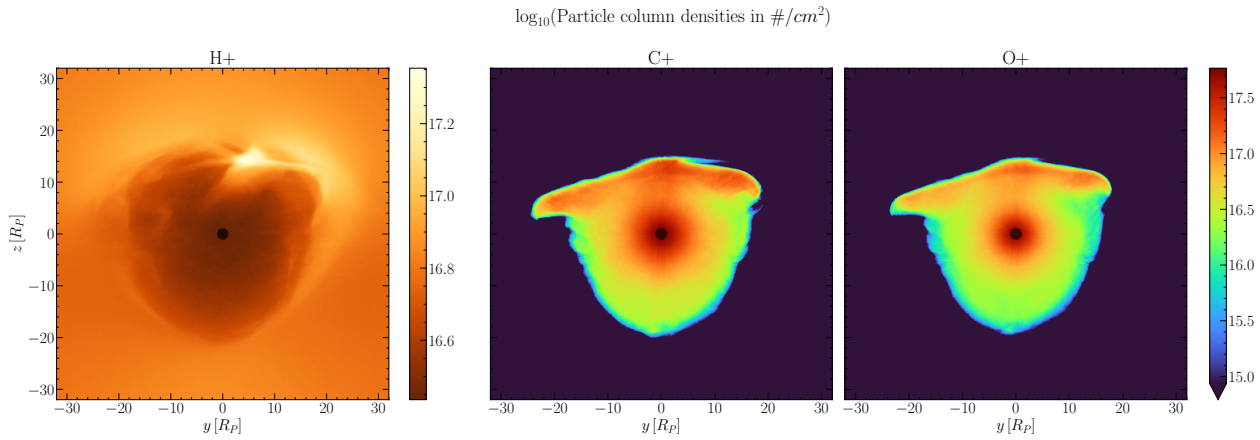

(a) No dipole

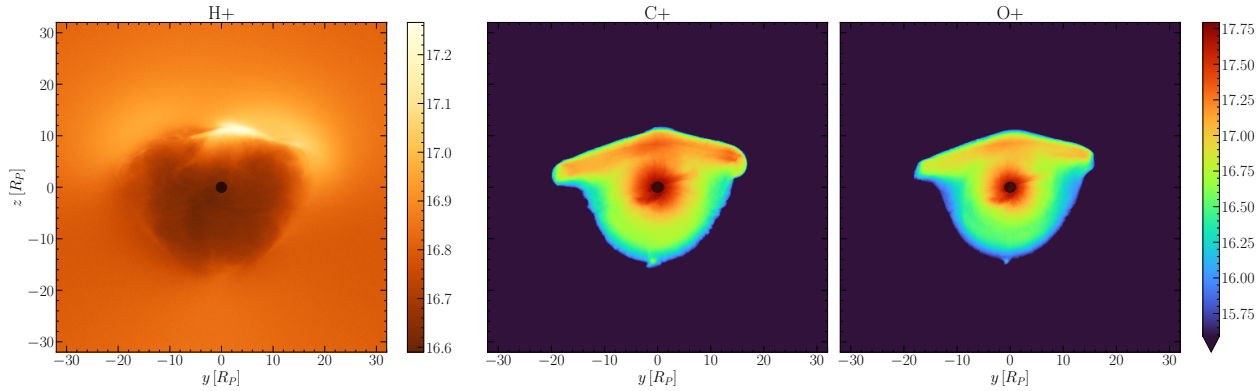

(b) Weak dipole

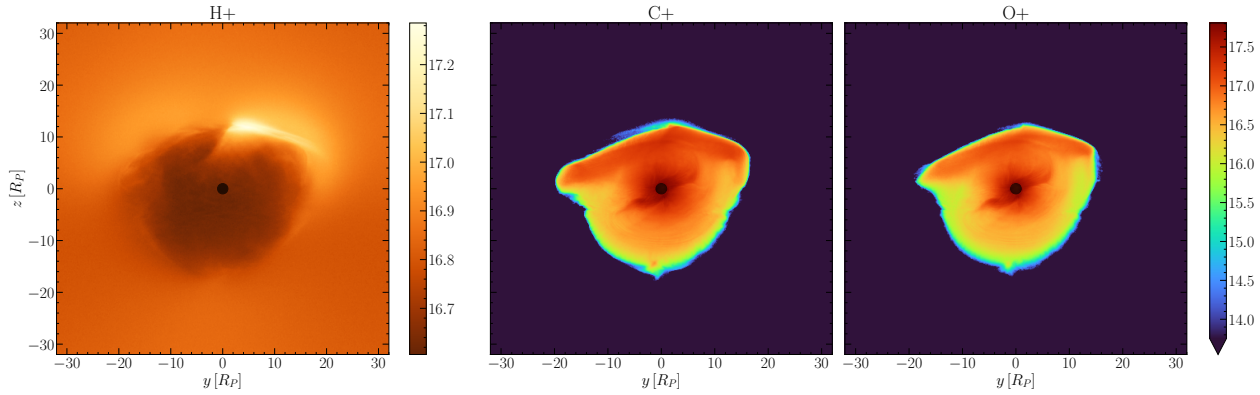

(c) Medium dipole

Figure 1: Column density of π Men c models with different magnetic field strengths.